

The Kennaugh element framework for multi-scale, multi-polarized, multi-temporal and multi-frequency SAR image preparation



Andreas Schmitt ^{a,*}, Anna Wendleder ^a, Stefan Hinz ^b

^a German Aerospace Center (DLR), German Remote Sensing Data Center (DFD), Land Surface Applications, Oberpfaffenhofen, D-82234 Weßling, Germany

^b Karlsruhe Institute of Technology (KIT), Institute of Photogrammetry and Remote Sensing (IPF), Englerstr. 7, D-76131 Karlsruhe, Germany

ARTICLE INFO

Article history:

Received 30 April 2014

Received in revised form 9 October 2014

Accepted 14 January 2015

Available online 14 February 2015

Keywords:

Radar
SAR
Imagery
Multifrequency
Multisensor
Multitemporal
Multiresolution
Change detection
Application
Combination
Polarization

ABSTRACT

As the number of space-borne SAR sensors increases, a rising number of different SAR acquisition modes is in use, resulting in a higher variation within the image products. This variability in acquisition geometry, radiometry, and last but not least polarimetry raises the need for a consistent SAR image description incorporating all available sensors and acquisition modes. This paper therefore introduces the framework of the Kennaugh elements to comparably represent all kinds of multi-scale, multi-temporal, multi-polarized, multi-frequency, and hence, multi-sensor data in a consistent mathematical framework. Furthermore, a novel noise model is introduced that estimates the significance and thus the (polarimetric) information content of the Kennaugh elements. This facilitates an advanced filtering approach, called multi-scale multi-looking, which is shown to improve the radiometric accuracy while preserving the geometric resolution of SAR images. The proposed methodology is finally demonstrated using sample applications that include TerraSAR-X (X-band), Envisat-ASAR, RADARSAT-2 (C-band) and ALOS-PALSAR (L-band) data as well as the combination of all three frequencies. Thus the suitability of the Kennaugh element framework for practical use is proved for advanced SAR remote sensing.

© 2015 The Authors. Published by Elsevier B.V. on behalf of International Society for Photogrammetry and Remote Sensing, Inc. (ISPRS). This is an open access article under the CC BY-NC-ND license (<http://creativecommons.org/licenses/by-nc-nd/4.0/>).

1. Introduction

The first section links the motivation and the related work to the “multi” terms that define the frame of this contribution: multi-temporal, multi-scale, multi-polarized, multi-frequency, and multi-sensor.

1.1. Motivation

With the ongoing development and improvement of air- and space-borne SAR sensors, the variety of imaging modes, processing and image analysis approaches increases steadily. Along with this, also the range of applications widens up. Yet, the algorithmic developments over the past years led to a vast diversity of SAR image analysis and evaluation strategies. Their focus on very specific aspects is difficult to overview and hence a stronger impact on practical applications of remote sensing seems to be limited. With the development of highly sophisticated and flexible SAR instruments, the need for generic algorithmic frameworks that can deal with this flexibility gets even bigger. Thus, a main

contribution of our approach refers to the fact that it can cope with very different input data without the need of being modified. It relies on a very simple, but versatile technique that combines any focused SAR image in a consistent mathematical framework. It ensures a wide range of feasible applications thanks to a very careful data handling. Therefore, it is essential that this novel technique complies with certain requirements: multi-sensor, multi-frequency, multi-scale, multi-polarized, and multi-temporal which will be introduced in the following.

The availability of SAR acquisitions is always limited by the durability and the utilized capacity of the corresponding sensor. Regarding former sensors like ERS-1 & -2 providing long-term SAR data back to the 1990s, the joint preparation of data acquired by different sensors gains more and more interest to establish time series over more than two decades. In view of current sensors, the availability of SAR data for time-critical applications still is difficult. It could be improved if the acquisitions of different sensors were processed and delivered in the same image product type. With this method, temporarily unavailable sensors can easily be replaced by others. Hence, an advanced SAR processing framework should be designed towards “multi-sensor”. This point often implies “multi-frequency” as well because the wavelength in general varies with the sensor. Instead of ordinarily replacing the

* Corresponding author.

one by the other sensor, the combination of multi-frequent images acquired contemporaneously promises a better target discrimination especially for distributed or natural targets (McNairn et al., 2014).

1.2. Image processing background

The first challenge of combining several sensors is to define a joint coordinate system in which all data sets are projected. As SAR imaging geometry is highly variable, an ortho-rectified version in the UTM coordinate system is chosen instead of sensor geometries (Huber et al., 2004). The geocoding process requires highly accurate – post-processing – orbit information as well as a detailed globally available elevation model. Then, further co-registration is dispensable. Nowadays a mosaic of SRTM and GLOBE is used for geocoding. In future the TanDEM-X digital elevation model will be state-of-the-art. The problem of unifying multiple scales is solved simultaneously by using the same sampling distance during projection (Schmitt et al., 2010). Thus, the resulting images though sharing the same location and pixel spacing unify different look numbers – in other words “scales” of the original images. This initial multi-looking depends on the original geometric resolution in slant range and azimuth, the incidence angle, etc. and is essential in order to prevent information loss by subsampling. A further meaning of the “multi-scale” characteristic is given by the selective variation of the look numbers during the image enhancement process called “multi-scale multi-looking”. Instead of estimating a nominal look number being appropriate for the whole coverage – which is not possible (Lee et al., 1994; Touzi, 2002) – the optimal image scale is chosen locally according to the image content. Coarser scales are selected for distributed targets, and the finest scale is chosen for point targets. Thereby, several scales of the same image are combined in one single image product in favor of the radiometric accuracy.

The term “multi-polarized” aims at the capability of representing any kind of polarization combination possible in a consistent mathematical framework. The standard way of processing multi-polarized acquisitions is considering the amplitude images exclusively. Beside that, numerous polarimetric decompositions have been developed additionally exploiting the phase information of quad-pol images (Cloude and Pottier, 1996; Touzi et al., 2004). In general, those cannot be utilized for dual-pol images except for some approaches that explicitly have been adapted to special sensor modes (Cloude, 2006; Shan et al., 2011; Ullmann et al., 2013; Lopez-Sanchez et al., 2012). Apart from that, all decompositions are either coherent or incoherent. On the one hand coherent decompositions base on the Sinclair matrix which prohibits any multi-looking step needed for the description of distributed targets (Lee and Pottier, 2009). On the other hand incoherent decompositions based on either the covariance or the coherency matrix often require large look numbers in order to guarantee radiometric stability (Touzi, 2007). Thus, the geometric resolution of the image degrades considerably. A basic description of the backscattering process by the elements of the well-known Kennaugh matrix hence seems to be the right balance. Always consisting of the total intensity and a varying number of polarimetric channels according to the measured polarization channels the Kennaugh element description is suitable for all kind of polarization combinations. Intensity and polarimetric information can easily be detached by employing the normalized variant of the Kennaugh matrix (Schmitt and Brisco, 2013). With reference to the number of looks, the Kennaugh matrix is capable to describe both coherent and incoherent scattering (Cloude, 2009). There are no restrictions concerning the look number which means furthermore that the geometric resolution can arbitrarily be chosen with respect to the expansion of the targets of interest. Last but not least, the pre-processing in Kennaugh elements still enables the subsequent decomposition by any algorithm preferred for special applications.

Because of their linear relationship the Kennaugh matrix can easily be transformed into the coherency or covariance matrix which acts as basis for common incoherent polarimetric decompositions.

1.3. Evaluation of image sequences

As soon as several images of the same region are acquired the questions arises whether there have been changes to the landscape in the mean-time or not. Two strategies have been published so far: the simple change detection taking a binary decision whether there was a change or not (Conradsen et al., 2003; Bovolo and Bruzzone, 2005; Bouyahiaa et al., 2008; Liao et al., 2008; Erten et al., 2012; Marino et al., 2013) which mainly focuses on abrupt changes caused by unexpected impacts (e.g. earth quakes, floods, fires), and secondly, the generation of large image stacks incorporating the single time slots so that the development of single pixels or regions (e.g. the phenological development of agricultural land) can be derived (Marcos et al., 2007; Leichtle, 2013; Alonso-González et al., 2014; Metz and Marconcini, 2014), commonly referred to as time series analysis. With image stacks in mind, the persistent scatterer interferometry (Ferretti et al., 2001) that measures slightest geometrical movements for strong and stable targets has to be mentioned. It is ranked among the interferometric approaches which are not focus of this contribution due to their very high sensitivity to co-registration errors and atmospheric conditions (Moreira et al., 2013).

In this paper, a novel “multi-temporal” image product is introduced. It assumes the radiometric stability of a scene over time and carves out any variation be it on the intensity or polarimetry. In contrast to Marino et al. (2013), no single change measure allowing for a binary decision is derived. But all channels are addressed separately in order to gain maximum information content. Additionally, there is no minimum look number required with our approach, i.e. geometric resolution is preserved. Meanwhile Marino et al. (2013) report on look numbers of more than one hundred which indicate the inflation of the reasonable pixel size to ten times the original in both dimensions. In the style of normalized Kennaugh elements, where all measurements are related to the total intensity, differential Kennaugh elements are defined that describe the relative and continuous deviation of two images acquired at different times (“multi-temporal”), in different scales (“multi-scale”), or by different sensors (“multi-sensor”). The images are jointly enhanced by the multi-scale multi-looking procedure based on the joint intensity image in order to achieve best geometric resolution and therewith, best radiometric accuracy. This joint intensity image is evaluated for the generation of the optimal look image. Additionally, the noise model allows for the estimation of the significance of differential as well as polarimetric Kennaugh elements with respect to the number of looks, the intensity, and the noise floor. Thus, using this technique, temporal changes cannot only be detected, but furthermore characterized by their significance, their strength or their polarimetric behavior (Brisco et al., 2011).

In conclusion, the Kennaugh element framework offers a very flexible technique for all kind of SAR data preparation and practical application. This approach tends to the optimal data handling in terms of geometric resolution and radiometric accuracy, in short: data quality. The following chapters will introduce the methodological background analytically and stochastically. Afterwards, some examples and closing remarks complete this contribution.

2. Theory and methodology: analytical aspects

This chapter derives the four characteristics of the new descriptor: multi-polarized, multi-temporal, multi-scale, and multi-sensor.

Descriptor in this sense refers to the set of information layers available with each image pixel, i.e. the information depth. Starting with the Kennaugh matrix the conditions and formulas for different polarization combinations available nowadays are derived. Afterwards, the Kennaugh element theory is extended to multi-temporal acquisitions by combining several images in one. At last, even different sensors are merged together in order to highlight multi-frequency deviations.

2.1. Multi-polarized Kennaugh elements

The traditional Kennaugh matrix is the linear transformation of the four-dimensional Stokes vector – i.e. a real four-by-four scattering matrix – in the backscatter-alignment coordinate system. It consists of the total intensity, quasi the “scaling factor”, and fifteen intensity differences representing the fifteen linear coefficients of the transformation. As for monostatic sensor configurations the cross-polar channels are identical due to the theorem of reciprocity, the Kennaugh matrix becomes symmetric and the number of independent entries reduces to ten (Boerner, 2010). In order to guarantee symmetry the elements of the symmetric Kennaugh matrix K are derived via $K = \frac{1}{2}(K_S + K_S^T)$ from the standard formulas of a general Kennaugh matrix K_S and further analytical simplifications. The denotation unfolds to

$$[K] = \begin{bmatrix} K_0 & K_4 & K_5 & K_6 \\ K_4 & K_1 & K_9 & K_8 \\ K_5 & K_9 & K_2 & K_7 \\ K_6 & K_8 & K_7 & K_3 \end{bmatrix} = I \cdot \begin{bmatrix} 1 & k_4 & k_5 & k_6 \\ k_4 & k_1 & k_9 & k_8 \\ k_5 & k_9 & k_2 & k_7 \\ k_6 & k_8 & k_7 & k_3 \end{bmatrix} = I \cdot [k] \quad (1)$$

where lowercase letters refer to the normalized Kennaugh matrix k after division by the total intensity I which is equal to K_0 . All normalized Kennaugh elements range in-between -1 and $+1$ in the so-called hyperbolic tangent scaling (see Appendix A.1) which can be interpreted as scaled difference of two logarithmic amplitudes.

$$k_i = \tanh(\ln A_a - \ln A_b) = \frac{I_a - I_b}{I_a + I_b} = \tanh\left(\frac{\ln 10}{20} k_{i[dB]}\right) \quad i = 1, \dots, 9 \quad (2)$$

Alternatively, it can be seen as quotient of the difference by the sum of two intensities, e.g. the co- and the cross-pol intensities for the Kennaugh element k_i . Additionally, there is a direct link to the measure in the common unit decibel. In the same way, the total intensity can be normalized by introducing the reference intensity of 1. Furthermore, it can be proven that $a \tanh k_0$ is proportional to the logarithmic intensity in decibel and the proportionality constant is equal to $\frac{\ln 10}{20}$.

$$k_0 = \tanh(\ln A) = \frac{I - 1}{I + 1} = \tanh\left(\frac{\ln 10}{20} I_{[dB]}\right) \quad (3)$$

Thus, all Kennaugh elements can be described in the same scaling whether linear, logarithmic, or normalized scale. This is a great advantage in contrast to other polarimetric descriptors where various units like power, angle, or unit-less entropy measures get mixed-up (Cloude and Pottier, 1997; Touzi et al., 2009). For display or storing reasons the normalized elements are preferred because of their closed value range and advantageous sampling rates when converting them to integer values, see Appendix A.2.

2.1.1. Single-pol images

In the single-pol case the only suitable information is captured in the intensity. The phase exclusively holds information when combining several repeat pass acquisitions to interferometric pairs (Bamler and Hartl, 1998; Moreira et al., 2013) which is not the focus of this paper. Thus, only the Kennaugh element K_0 remains which is

defined as summarized intensity of the measured image channels, e.g. $K_0 = |S_{HH}|^2$ for horizontally transmitted and horizontally received waves, typically called HH, or $K_0 = |S_{VV}|^2$ for vertical transmission and vertical reception, typically called VV. K_0 representing the total intensity is available with any polarimetric combination.

2.1.2. Dual-pol images

Regarding dual-pol modes three different combinations are common to today's SAR sensors predominantly using linear polarization: HH and VV polarization without fix inter-channel phase shift (Twin), HH & VV channels with fix inter-channel phase shift (Co-pol), and the transmission in one and reception in two perpendicular polarizations, e.g. HH & VH or VV & HV respectively (Cross-pol).

In the case of the Twin polarization, the phase difference being totally stochastic in default of a fix phase reference does not hold any information. Therefore, the intensities of both input channels $|S_{HH}|^2$ and $|S_{VV}|^2$ are the only source of information. If all elements containing channels that are neither measured nor holding distinct information are set to zero, then the Kennaugh elements K_0 and K_4 calculated as sum and as difference of the input intensities remain:

$$\begin{aligned} K_0 &= \frac{1}{2} \{ |S_{HH}|^2 + |S_{VV}|^2 \} \\ K_4 &= \frac{1}{2} \{ |S_{HH}|^2 - |S_{VV}|^2 \} \end{aligned} \quad (4)$$

K_0 reflects the total intensity while K_4 gives the difference between horizontal and vertical reflection that can be referred to different phenomena. At first, K_4 reflects the relation between horizontally and vertically oriented dipoles. Another reason for K_4 being different from zero might be the Bragg surface scattering that generally causes higher intensities in VV than in HH. A similar phenomenon can be caused by the Brewster angle effect occurring with double bounce scattering produced by trunks on ground (e.g.).

Co-pol acquisitions contain exactly the same polarization channels as Twin-pol images when delivered. But, in contrast to these the phase difference between both image channels can be evaluated thanks to a fix phase reference. Thus, the Kennaugh elements K_3 and K_7 – the real and the imaginary part of the inter-channel correlation – join the purely intensity-based elements K_0 and K_4 :

$$\begin{aligned} K_0 &= \frac{1}{2} \{ |S_{HH}|^2 + |S_{VV}|^2 \} \\ K_3 &= -Re\{S_{HH}S_{VV}^*\} \\ K_4 &= \frac{1}{2} \{ |S_{HH}|^2 - |S_{VV}|^2 \} \\ K_7 &= Im\{S_{HH}S_{VV}^*\} \end{aligned} \quad (5)$$

The interpretation of K_0 and K_4 stays exactly the same. K_3 contains the difference between even- and odd-bounce scattering which play a key role in the Pauli decomposition as well as in the coherency matrix and all further decompositions (Unal and Lighart, 1998; Alberga, 2004). K_7 holds the inter-channel correlation showing the phase difference between the odd- and even-bounce scattering event.

The typical cross-pol configuration is the transmission in one and the reception in two linear polarizations, e.g. transmitting horizontally and receiving both horizontally and vertically produces the image channels HH & VH which lead to following Kennaugh elements:

$$\begin{aligned} K_0 &= |S_{HH}|^2 + |S_{VH}|^2 \\ K_1 &= |S_{HH}|^2 - |S_{VH}|^2 \\ K_5 &= Re\{S_{HH}S_{VH}^*\} \\ K_8 &= Im\{S_{HH}S_{VH}^*\} \end{aligned} \quad (6)$$

If the transmitting polarization is switched to vertical polarization, then the channels VV & HV are measured. Anyway, the same Kennaugh elements

$$\begin{aligned} K_0 &= |S_{VV}|^2 + |S_{HV}|^2 \\ K_1 &= |S_{VV}|^2 - |S_{HV}|^2 \\ K_5 &= \operatorname{Re}\{S_{HV}S_{VV}^*\} \\ K_8 &= -\operatorname{Im}\{S_{HV}S_{VV}^*\} \end{aligned} \quad (7)$$

can be derived. Preliminary studies even proofed that the impact of the transmitting polarization is almost negligible because of the very high correlation between the Kennaugh elements calculated from HH & VH and those calculated from VV & HV polarization.

Again, the Kennaugh elements derived from these two input channels can be divided in two intensity-only channels K_0 and K_1 as well as two channels containing the real and the imaginary parts of the inter-channel correlation K_5 and K_8 . The total intensity can be found in K_0 . The difference between co- and cross-polarized intensity appears in K_1 . In general the co-polarized intensity exceeds the cross-polarized intensity except for strong volume targets like forest. The discrimination of intensity-only and phase-based elements is very essential for the radiometric stability of the Kennaugh elements. In general, the phase shift between co- and cross-polarized channels becomes completely stochastic over natural targets (Freeman and Durden, 1998; Hong and Wdowinski, 2013). One reason for that is the reflection symmetry in the case of natural targets being equally distributed with respect to the line of sight. Another reason is the discrepancy of the phase centers during reflection. The elements K_5 and K_8 consequently hold useful information for deterministic – usually man-made – targets exclusively. In eigen-vector based decompositions (Cloude and Pottier, 1996; Touzi et al., 2004) those effects get completely mixed resulting in very noisy decomposition parameters and thus, requiring very high look numbers to overcome this problem. Other decompositions trying to interpret the correlation of the co- and cross-polarized channels potentially impair the description of natural targets (Cameron et al., 1996; Lee et al., 1999; Yamaguchi et al., 2005).

2.1.3. Hybrid compact-pol images

For inter-planetary missions like the mapping of the Mars surface the compact-pol mode has already been employed (Raney, 2011). But also for future earth observation sensors the compact-pol mode is of interest and has been investigated several times in pilot studies. The idea behind this sensor configuration is to apply different polarization types for transmission and reception, e.g. transmitting circularly polarized light while receiving in two perpendicular linear polarizations. Regarding the hybrid compact-pol mode as published by Raney (2007) the transmitted wave is right circularly polarized while the reflected wave is received both in horizontal and vertical direction. Thus, the image channels S_{HR} and S_{VR} are measured. The RISAT sensor being the only satellite currently offering this mode, the compact-pol image mostly is simulated based on a quad-pol image via

$$\begin{aligned} S_{HR} &= \frac{S_{HH} - \frac{i}{2}(S_{HV} + S_{VH})}{\sqrt{2}} \\ S_{VR} &= \frac{\frac{1}{2}(S_{HV} + S_{VH}) - iS_{VV}}{\sqrt{2}} \end{aligned} \quad (8)$$

according to Charbonneau et al. (2010). Replacing the standard linear polarization channels by these hybrid compact channels results in the four independent Kennaugh elements

$$\begin{aligned} K_0 &= |S_{HR}|^2 + |S_{VR}|^2 \\ K_3 &= -\operatorname{Im}\{S_{HR}S_{VR}^*\} \\ K_5 &= \operatorname{Re}\{S_{HR}S_{VR}^*\} \\ K_8 &= |S_{VR}|^2 - |S_{HR}|^2 \end{aligned} \quad (9)$$

whereof K_0 and K_8 are intensity-only elements and K_3 and K_5 reflect the inter-channel correlation. Similar results – the same Kennaugh

elements though different input channels – can be achieved using left circular transmitting waves instead of right circular. K_0 again reflects the total intensity while the interpretation of the others still has to be further explored.

2.1.4. Quad-pol images

Quad-pol acquisitions deliver all image channels needed for a complete description of the polarimetric scattering. Therefore, all ten Kennaugh elements can be calculated. The formulas

$$\begin{aligned} K_0 &= \frac{1}{2} \{|S_{HH}|^2 + |S_{HV}|^2 + |S_{VH}|^2 + |S_{VV}|^2\} \\ K_1 &= \frac{1}{2} \{|S_{HH}|^2 - |S_{HV}|^2 - |S_{VH}|^2 + |S_{VV}|^2\} \\ K_2 &= \frac{1}{2} (|S_{HV}|^2 + |S_{VH}|^2) + \operatorname{Re}\{S_{HH}S_{VV}^*\} \\ K_3 &= \frac{1}{2} (|S_{HV}|^2 + |S_{VH}|^2) - \operatorname{Re}\{S_{HH}S_{VV}^*\} \\ K_4 &= \frac{1}{2} \{|S_{HH}|^2 - |S_{VV}|^2\} \\ K_5 &= \frac{1}{2} \operatorname{Re}\{S_{HH}S_X^* + S_XS_{VV}^*\} \\ K_6 &= \frac{1}{2} \operatorname{Im}\{S_{HH}S_X^* + S_XS_{VV}^*\} \\ K_7 &= \operatorname{Im}\{S_{HH}S_{VV}^*\} \\ K_8 &= \frac{1}{2} \operatorname{Im}\{S_{HH}S_X^* - S_XS_{VV}^*\} \\ K_9 &= \frac{1}{2} \operatorname{Re}\{S_{HH}S_X^* - S_XS_{VV}^*\} \end{aligned} \quad (10)$$

result from the symmetrization and further simplification of the standard Kennaugh matrix. Where necessary, the cross-polarized channels are summed up to $S_X = S_{HV} + S_{VH}$ for the sake of clarity. The linear polarization base was chosen because it is still the most common polarization base of SAR sensors. Nevertheless, the Kennaugh matrix can be derived from any polarimetric measurement in an arbitrary polarization basis. Even if circular polarization replaces linear polarization as standard polarization in the future, the Kennaugh descriptor will still be valid, c.f. Section 2.1.3. Furthermore, any other (incoherent) scattering matrix can be derived from the Kennaugh elements if necessary for subsequent decomposition (Anderson and Barakat, 1994; Espinosa-Luna et al., 2008).

It has to be noted that the interpretation of the individual Kennaugh elements is not quite simple. Two theories have been discussed in literature so far: the Huynen interpretation (Huynen, 1970) common to SAR applications and the traditional interpretation from optical polarimetry dividing the elements in three groups and three coordinate axes (Le Roy-Bréhonet et al., 1996; Kerwien, 2007). The coordinate systems are oriented parallel to the linear axes, i.e. horizontally and vertically (K_1, K_4, K_7), diagonal to the linear axes, i.e. in 45° and 135° (K_2, K_5, K_8), and circular in right and left rotating direction (K_3, K_6, K_9). The first group is composed out of the absorption elements K_1, K_2, K_3 that describe the loss of polarization during the scattering process. The second group consisting of the elements K_4, K_5, K_6 is called diattenuation, i.e. the change of the relation between two amplitude values, e.g. HH and VV for K_4 , during reflection. The third group unifies the retardance elements K_7, K_8, K_9 which describe the phase delay during scattering in the respective direction, e.g. circular phase delay for K_9 .

The polarization content \mathcal{P}_G of the individual layers or groups of layers, i.e. their polarimetric information contribution, can easily be calculated via

$$\mathcal{P}_G = \sqrt{\frac{1}{n} \sum_1^n k_i^2} \quad i \in [1, 2, 3, 4, 5, 6, 7, 8, 9] \quad (11)$$

quasi as standard deviation of the normalized polarimetric Kennaugh elements. For instance, the polarization content P_1 of K_1 is given by $i = 1$, while the polarization content of the diattenuation elements P_{diat} is defined by $i = 4, 5, 6$. In the same way the Kennaugh elements for a certain orientation can be derived, e.g. $P_{circular}$ composes of $i = 3, 6, 9$. The total polarization of a Kennaugh matrix P_{total} consequently results from the combination of all polarimetric Kennaugh elements $i = 1, \dots, 9$. Regarding the multi-temporal Kennaugh elements which will be introduced in the following section, even the amount of change between two time slots can be characterized by the measure P_{change} also for various combinations of the differential Kennaugh elements as defined in Eq. (11) which is fundamental for change detection.

The total intensity K_0 – or rather total absorption from the view of optical polarimetry – defined as sum over all intensity channels in the case of SAR measurements is directionless by nature. This interpretation also defines the basis for several decompositions of the Mueller matrix used in optics (Lu and Chipman, 1996; Ossikovski, 2008; Ossikovski et al., 2008; Boulvert et al., 2009) which show a striking similarity to the decompositions employed in SAR polarimetry (Praks et al., 2009).

2.2. Multi-temporal and multi-frequency Kennaugh elements

With the increasing availability of SAR images the multi-temporal aspect gains more and more attention. Thus, not only the state, but the temporal development – in the simplest case the change from one to another acquisition – is of interest when evaluating SAR observations. Today's standard approaches start with two multi-looked and sometimes even speckle-filtered images and try to develop algorithms that highlight distinct changes by reducing the huge number of false alarms (Carincotte et al., 2006). Instead of comparing two separate images, the multi-temporal acquisitions are gathered in one image product and jointly enhanced in order to gain best radiometric accuracy. Radiometric accuracy in general depends on three parameters: the sensor and mode specific noise floor (additive noise), the look number (smoothing), and the intensity itself (multiplicative noise) (Elachi, 1988). Therefore, the total intensity layer is calculated with each multi-temporal product composed out of all the input intensities K_0^a and K_0^b weighted by the respective number of looks L^a and L^b . This intensity layer

$$K_0^{a\&b} = \frac{L^a \cdot K_0^a + L^b \cdot K_0^b}{L^a + L^b} \quad (12)$$

reflects the best available intensity image in terms of image quality and acts as optimal basis for image enhancement. Regarding multi-temporal image stacks this K_0 layer can be compared to the multi-temporal coherency matrix that generates a multi-look description without losing geometric resolution (Navarro-Sánchez and Lopez-Sánchez, 2014). Doing so, even the quality of the polarimetric Kennaugh elements k_{1-9} can be improved without suffering from imbalances in-between the multi-temporal elements caused by varying intensities and/or look numbers.

For the comparison of multi-temporal Kennaugh elements it is essential to define in advance that a continuous measure displaying the relative changes unbiased by variations in intensity or different look numbers is of interest. Thus, the independent normalized Kennaugh elements – expressed in vector \vec{k} – have to be compared in the logarithmic scale (similar to the difference in dB) or alternatively as normalized elements generating multi-temporal “differential” Kennaugh elements as follows:

$$dk^{a-b} = \tanh(\operatorname{atanh}\vec{k}^b - \operatorname{atanh}\vec{k}^a) = \frac{\vec{k}^b - \vec{k}^a}{1 - \vec{k}^a \cdot \vec{k}^b} \quad (13)$$

Advantageously, for the change of the total intensity the logarithmic version of the new differential Kennaugh element dk_0^{a-b} is identical to the well-known logarithmic amplitude quotient (c.f. Eq. (2)). Therefore, it can equivalently be expressed in decibel as usual. The same goes for differential polarimetric Kennaugh elements dk_{1-9}^{a-b} . If the multi-temporal images are replaced by multi-sensor acquisitions, e.g. in order to close temporal gaps or to acquire multi-frequency data, the same formulation derived above (see Eqs. (12) and (13)) can be applied. The differential Kennaugh elements of one TerraSAR-X and one RADARSAT-2 acquisition for instance highlight the different backscattering in X- and C-band as well as temporal changes. Additionally, when relying on the combined intensity image during the image enhancement process the maximum geometric resolution is retained for both input images even though there might be a high discrepancy in the look numbers.

2.3. Multi-scale Kennaugh elements

In terms of filtering multi-polarized SAR data it is important to underline that image enhancement should be based on a conservative potential field which is only present in intensity values, e.g. the total intensity of the Kennaugh representation (Raney, 1998). Thus, the multi-scale intensities are compared in order to select the optimal scale, i.e. the optimal look number, for all other multi-polarized and/or multi-temporal channels. Given two completely uncorrelated intensities the significance scaling function is easy to simulate, see Section 3.2. In the case of multi-scale intensities correlations are inevitable, see Fig. 1. The fine-scale intensity I_{fine} is completely contained in the coarse scale I_{coarse} . In order to exclude correlations the inner circle I_b of Fig. 1 must be separated from the outer circle symbolizing I_a .

When differencing the fine intensity incorporating m looks and the coarse-scale intensity incorporating n looks, it can be proven that the resulting difference is proportional to the difference of the uncorrelated intensities I_a and I_b , see Appendix A.4 for more explanations. In order to generate a normalized Kennaugh element, the difference has to be related to the sum of both intensities. As the value of the fine intensity would gain too much weight when summing up the fine and the coarse intensities, its influence has to be reduced by a weighted mean, see Appendix A.5. Fortunately, the proportionality factor cancels down when the multi-scale differential Kennaugh element is derived as follows.

$$dk_0^{fine-coarse} = \frac{I_a - I_b}{I_a + I_b} = \frac{I_{coarse} - I_{fine}}{I_{coarse} + I_{fine} \cdot (1 - 2 \cdot \frac{m}{n})} \quad (14)$$

The look number of the combined intensity, which is fundamental for the significance estimation of a Kennaugh element, composes as doubled harmonic mean of the looks of the fine scale and the look difference between coarse and fine scale:

$$L = \frac{4}{\frac{1}{n-m} + \frac{1}{m}} \quad (15)$$

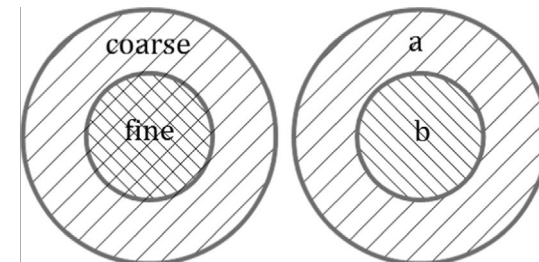


Fig. 1. The intersection of multi-scale intensities in the image domain.

The proof can be found in [Appendix A.3](#). The harmonic mean likewise is applied when combining uncorrelated multi-scale data with varying look numbers e.g. multi-sensor data. In summary, as soon as the correlation of two intensity values is known (e.g. with multi-scale intensities), they can be combined to a differential Kennaugh element of uncorrelated input variables. Thus, it is sufficient to investigate the stochastic behavior of the pure and unbiased Kennaugh elements in the following section.

3. Theory and methodology: statistical aspects

The statistical behavior of Kennaugh elements being defined as quotient of the difference of two intensity values by their sum is quite complicated to describe. Common models capture the distribution of intensity values, of their sum, or of their quotient ([López-Martínez and Fàbregas, 2008](#); [Lee and Pottier, 2009](#)). But, the difference of two intensity values though addressed in literature ([Cheng and Berger, 2003](#)) or further combinations of intensity values have never been used in SAR remote sensing. Hence, there is no accepted model that could describe the distribution of Kennaugh elements. Additionally, with the improvement of geometric resolution of SAR images the portion of distributed targets significantly reduces, i.e. traditional speckle models – in general limited to fully developed speckle – are no longer appropriate. Furthermore, most standard models need parameters extracted from the image's second order statistics like the standard deviation in a certain environment whose expansion is not definable in advance. Therefore, a new noise model should be independent of the image statistics, but anyways adaptable to any kind of intensity and polarimetric measurement regardless of the acquiring sensor configuration. In contrast to similar fully automatic image enhancement approaches published recently (e.g. [Alonso-González et al., 2014](#)) that solve the problem of parameter tuning iteratively in order to avoid manual interaction, our approach shall process the input data sequentially without any iteration in order to minimize computation time.

3.1. Calculation of perturbation

Instead of modeling the distribution of intensity values, this approach starts with the basics of the SAR image: the measured variables. Assuming that each measurement is perturbed by a certain noise contribution s , the perturbation of all derived variables can be calculated. Numerous simulations lead to the empirical distribution function which is approximated analytically. The significance of Kennaugh elements consequently is related to the noise floor, the look number, and the local intensity.

3.1.1. Complex measurement

In each SAR image the real and imaginary parts of the incoming wave are the original measurements. Therefore, the calculation of perturbation starts with the definition of the measured values

$$\begin{aligned} Re_{\text{measured}} &= Re_{\text{true}} + s_{Re} \\ Im_{\text{measured}} &= Im_{\text{true}} + s_{Im} \end{aligned} \quad (16)$$

that deviate from the true values Re_{true} and Im_{true} by a certain perturbation value s_{Re} and s_{Im} respectively. We assume these perturbations to follow a normal distribution with its mean in zero and a standard deviation which is unknown so far. From the perturbation of these basic measurements the perturbations of all derived variables can be estimated.

3.1.2. Phase

Starting with the phase information defined as arctangent of the measured imaginary part by the measured real part, the measured parameters are replaced by the real parameters and their

perturbations from Eq. (16). Finally, the true amplitude which is equal for the real and the imaginary part is factored out to get:

$$\begin{aligned} \tan \varphi_{\text{derived}} &= \frac{Im_{\text{measured}}}{Re_{\text{measured}}} = \frac{Im_{\text{true}} + S_{Im}}{Re_{\text{true}} + S_{Re}} = \frac{A_{\text{true}} \cdot \sin \varphi_{\text{true}} + S_{Im}}{A_{\text{true}} \cdot \cos \varphi_{\text{true}} + S_{Re}} \\ &= \frac{\sin \varphi_{\text{true}} + \frac{S_{Im}}{A_{\text{true}}}}{\cos \varphi_{\text{true}} + \frac{S_{Re}}{A_{\text{true}}}} \end{aligned} \quad (17)$$

The noise components being independent of the image intensity are divided by the real image amplitude. This fact points out that the phase measurements become more and more stable with increasing amplitudes. This fact is well-known and has often been observed in interferometric applications ([Hanssen, 2001](#)).

3.1.3. Intensity

The image intensity is much more interesting for our application. It composes of the squared real and imaginary part. The substitution of the measured values by the true values and their perturbations results in:

$$\begin{aligned} I_{\text{derived}} &= Re_{\text{measured}}^2 + Im_{\text{measured}}^2 = Re_{\text{true}}^2 + Im_{\text{true}}^2 + 2 \cdot Re_{\text{true}} \cdot S_{Re} \\ &\quad + 2 \cdot Im_{\text{true}} \cdot S_{Im} + S_{Re}^2 + S_{Im}^2 = I_{\text{true}} + 2 \cdot A_{\text{true}} \cdot (S_{Re} \cdot \cos \varphi_{\text{true}} \\ &\quad + S_{Im} \cdot \sin \varphi_{\text{true}}) + S_{Re}^2 + S_{Im}^2 \end{aligned} \quad (18)$$

Obviously there are two noise contributions to the measured intensity: an additive and a multiplicative contribution. The additive contribution only depends on the standard deviation of the perturbations. The purely additive noise – also known as noise floor or noise equivalent beta nought (NEBN) in SAR remote sensing – is usually delivered with each SAR product. The variance of the perturbations then can easily be estimated via $\sigma_s^2 = \frac{1}{2} \cdot NEBN$. The multiplicative noise depends on the perturbations, on the phase angles, and – in contrast to most other models – on the amplitude instead of the intensity ([Goodman, 1976](#)). This already indicates that the new noise model will be very sensitive in highly structured areas like urban environments where the density of deterministic targets is very high. The distribution of the phase angle φ being the last unknown in Eq. (18) above is assumed to be uniform between 0 and 2π . Thus the phase angle is completely stochastic as generally accepted for single SAR acquisitions.

3.2. The distribution of Kennaugh elements

The perturbation of direct measurements and derived intensities now is transferred to normalized Kennaugh elements. After developing the analytic description the distribution is simulated. Thanks to the closed value range, a special spreading function in dependence of the intensity, the look number, and the noise floor can be defined that generates a uniform distribution. Eventually the absolute values of the spread Kennaugh element directly reflect their probability.

3.2.1. The perturbation formulation

Kennaugh elements in general are composed of multi-look intensities. While the true values for intensity – and necessarily the amplitude as well – stay the same, the noise contributions are averaged over n looks. With increasing look number the multiplicative contribution reaches zero and the additive component converges to the noise floor for:

$$\begin{aligned} \bar{I}_{\text{derived}} &= \frac{1}{n} \sum_{i=1}^n I_{\text{derived}} = I_{\text{true}} + A_{\text{true}} \cdot \frac{2}{n} \sum_{i=1}^n (S_{iRe} \cdot \cos \varphi_{i\text{true}} + S_{iIm} \cdot \sin \varphi_{i\text{true}}) \\ &\quad + \frac{1}{n} \sum_{i=1}^n (S_{iRe}^2 + S_{iIm}^2) \end{aligned} \quad (19)$$

$$k_{\text{derived}} = \frac{A_{\text{true}} \cdot \left\{ \frac{1}{n} \sum_{i=1}^n (s_{iRe} \cdot \cos \varphi_{i\text{true}} + s_{ilm} \cdot \sin \varphi_{i\text{true}}) - \frac{1}{m} \sum_{j=1}^m (s_{jRe} \cos \varphi_{j\text{true}} + s_{ilm} \sin \varphi_{j\text{true}}) \right\} + \frac{1}{2} \left\{ \frac{1}{n} \sum_{i=1}^n (s_{iRe}^2 + s_{ilm}^2) - \frac{1}{m} \sum_{j=1}^m (s_{jRe}^2 + s_{ilm}^2) \right\}}{I_{\text{true}} + A_{\text{true}} \cdot \left\{ \frac{1}{n} \sum_{i=1}^n (s_{iRe} \cdot \cos \varphi_{i\text{true}} + s_{ilm} \cdot \sin \varphi_{i\text{true}}) + \frac{1}{m} \sum_{j=1}^m (s_{jRe} \cdot \cos \varphi_{j\text{true}} + s_{ilm} \cdot \sin \varphi_{j\text{true}}) \right\} + \frac{1}{2} \left\{ \frac{1}{n} \sum_{i=1}^n (s_{iRe}^2 + s_{ilm}^2) + \frac{1}{m} \sum_{j=1}^m (s_{jRe}^2 + s_{ilm}^2) \right\}} \quad (20)$$

It is known from Eq. (2) that each normalized Kennaugh element can be expressed as quotient of the difference by the sum of two intensity values. The substitution of the intensities by Eq. (19) then leads to the perturbation of a normalized Kennaugh element in Eq. (20). The true values accepted as equal are already canceled down. As the two intensities may even have different look numbers symbolized by m and n, the combined look number of the mean intensity has to be derived via the harmonic mean, see Appendix A.3.

Obviously the perturbation of a normalized Kennaugh element is very complex to derive analytically. In practice, the only known variables are the standard deviation of the perturbations (via the noise floor), the nominal look number (from standard multi-looking) and the derived intensities. The true values are generally unknown. Therefore the distribution of a normalized Kennaugh element is approximated by a Monte-Carlo simulation.

3.2.2. The simulated distribution

Looking at the parameters that affect the distribution, the stability of the normalized Kennaugh elements grows with increasing intensity and look number, and it reduces with increasing noise floor. Hence, the Kennaugh element becomes completely random for the combination of a high noise level, a very low intensity, and two single look intensities. Numerous simulations with varying looks, intensities, and noise floors show that a normalized Kennaugh element adopts a uniform distribution between -1 and $+1$ in this case. The cumulative distribution function becomes linear and the quantiles consequently are equidistant, c.f. bisectrix in Fig. 2. The Kennaugh elements thus show a linear unbiased correlation to their probability defined by $P(k) = 1 - |k|$ for completely random Kennaugh elements, e.g. the probability of a normalized deviation from zero of more than 0.9 is given by 10%. Otherwise the distribution approaches an S-like function which steepens in zero with increasing intensity (cf. Figs. 3–5) and increasing look

number (cf. the diverse black lines in Figs. 2–5) according to the numerous simulations.

3.2.3. The quantile-scaling function

Thanks to the closed value range between -1 and $+1$ of the normalized Kennaugh elements, their statistics show a very special behavior: the distribution function analogously can be used as spreading function or quantile-scaling function needed for the generation of a uniform distribution. In digital image processing this is well-known as histogram flattening or histogram equalization (Castleman, 1996) usually based on the empirical histogram. In contrast to that, the quantile-scaling function for normalized

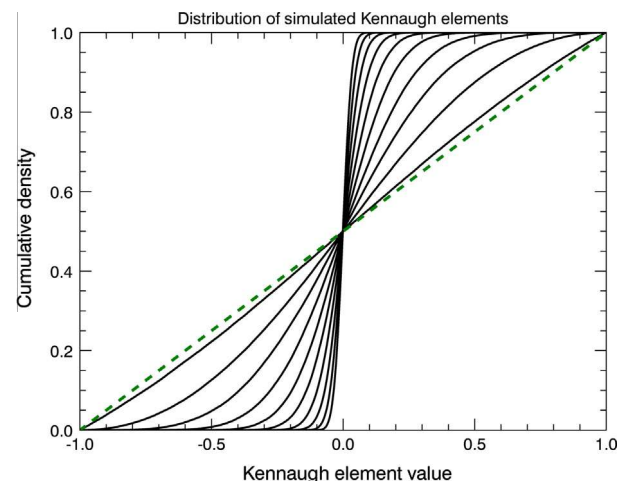


Fig. 3. Simulated distribution of normalized Kennaugh elements with a true intensity of -20 dB and varying look numbers $L \in [2, 4, 8, 16, 32, 64, 128, 256, 512, 1024]$ (noise floor -20 dB).

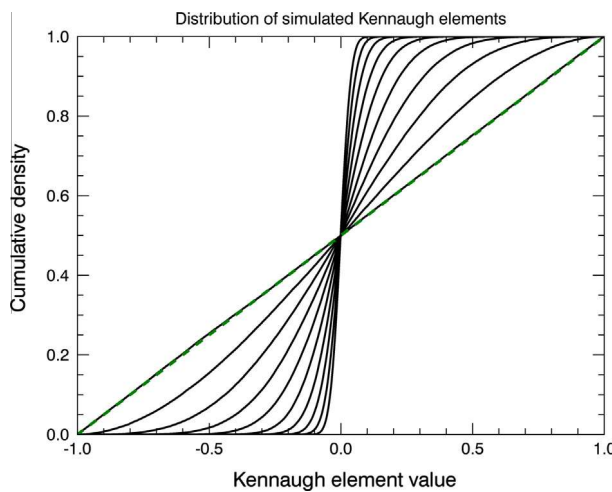


Fig. 2. Simulated distribution of normalized Kennaugh elements with a true intensity of -30 dB and varying look numbers $L \in [2, 4, 8, 16, 32, 64, 128, 256, 512, 1024]$ (noise floor -20 dB).

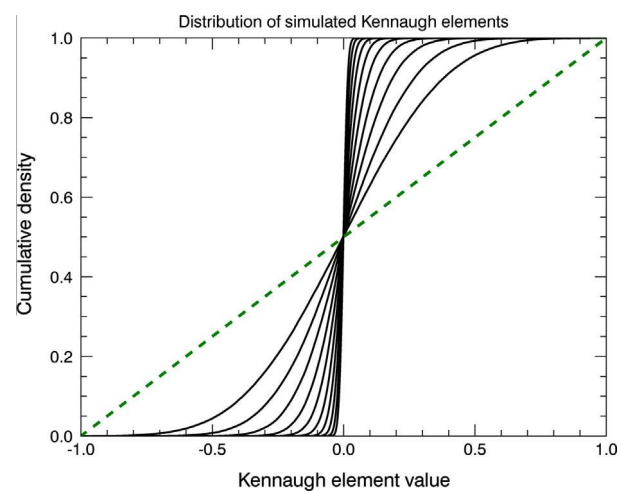


Fig. 4. Simulated distribution of normalized Kennaugh elements with a true intensity of -10 dB and varying look numbers $L \in [2, 4, 8, 16, 32, 64, 128, 256, 512, 1024]$ (noise floor -20 dB).

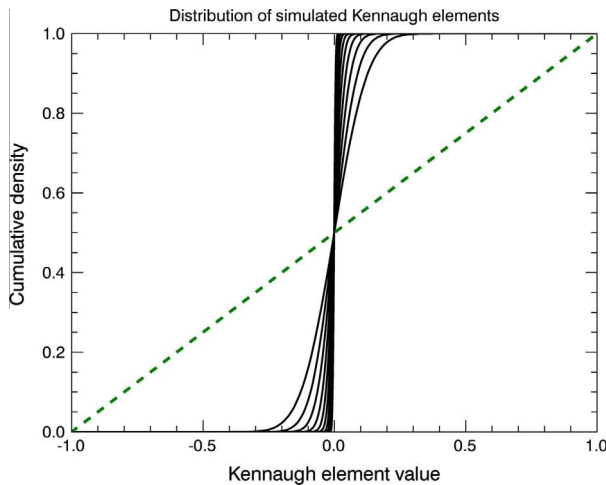


Fig. 5. Simulated distribution of normalized Kennaugh elements with a true intensity of 0 dB and varying look numbers $L \in [2, 4, 8, 16, 32, 64, 128, 256, 512, 1024]$ (noise floor –20 dB).

Kennaugh elements can be defined in advance by the perturbation-based noise model independently of any empirical and possibly biased image information. In the easiest case of completely random values this is already realized, i.e. the quantile-scaling function is equal to the bisectrix. With increasing intensity and/or look numbers (c.f. Figs. 2–5) the S-like distribution function steepens, thus the quantile-scaling function steepens likewise. In so doing the values of the Kennaugh elements beneficially can directly be interpreted as probability values.

The search for a suitable analytical approximation of the quantile-scaling function starts in the logarithmic scale. Obviously, a very steep peak in the logarithmic distribution produces a steep S-like function in the normalized distribution. Thus, the aim is to find a factor that spreads the logarithmic Kennaugh elements in a way that a uniform distribution is present in the normalized form. After some analytical simplifications and reformulations the approximation function can be defined as

$$k_{\text{scaled}} = \frac{(1 + k_{\text{derived}})^G - (1 - k_{\text{derived}})^G}{(1 + k_{\text{derived}})^G + (1 - k_{\text{derived}})^G} \quad (21)$$

where the control parameter G has to be estimated by the help of the available informations: derived intensity, looks, and noise floor. Numerous functions were tested many times empirically. The following definition delivered the best results for diverse intensities, looks, and noise in the typical value ranges.

$$\begin{aligned} G &= \frac{1}{2} \sqrt{\left(\frac{I}{I_R} + \frac{I_R}{I}\right)} \cdot \sqrt{\left(\frac{L}{L_R} - \frac{L_R}{L}\right)} \quad \text{with } I_R = \frac{\pi}{4} \cdot \text{NEBN} \text{ and} \\ L_R &= \frac{\pi}{4} \end{aligned} \quad (22)$$

Each run was performed using one million samples in order to guarantee smooth and reliable results reported in Figs. 6 and 7. Obviously, there are only negligible deviations from the ideal uniform distribution (bisectrix) after applying the quantile-scaling function. Regarding the interesting parts of the function – i.e. the 5% most significant values – the mean bias is below 0.05% and the standard deviation from the ideal values accounts less than 0.7%. Although the deviation seems to be larger around ± 0.5 (see Fig. 7), it never exceeds 2% which was found to be the maximum deviation over all simulation runs. Keeping in mind that the 99% percent quantile is typically used, this approximation certainly suffices.

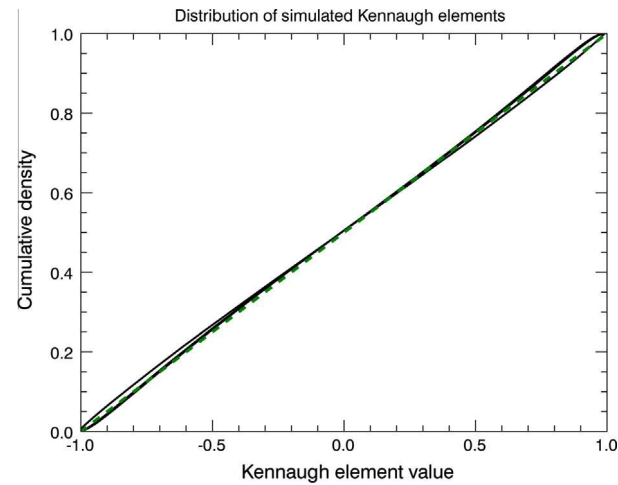


Fig. 6. Distribution of the Kennaugh elements after applying the analytical quantile-scaling function for a true intensity of –30 dB, a constant noise floor of –20 dB, and varying look numbers $L \in [1, 10, 100]$ in contrast to the bisectrix (equal distribution).

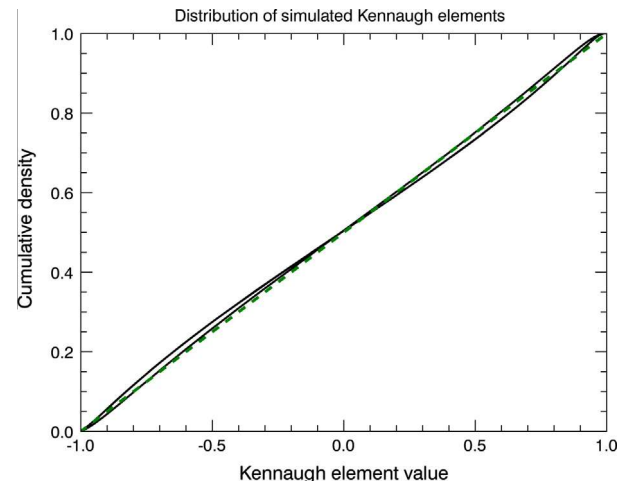


Fig. 7. Distribution of the Kennaugh elements after applying the analytical quantile-scaling function for a true intensity of 0 dB, a constant noise floor of –20 dB, and varying look numbers $L \in [1, 10, 100]$ in contrast to the bisectrix (equal distribution).

3.3. Multi-scale multi-looking

The preceding section explains in-depth the difficulties with noise handling in SAR images. In general, the only noise reducing operation for SAR intensity images is multi-looking. As there is no uniform look number being appropriate for the whole image, a multi-scale image representation – i.e. with locally varying look numbers – is envisaged in the following.

3.3.1. The image pyramid

The image pyramid (Adelson et al., 1984) is a trade of geometric resolution against radiometric accuracy. While the finer scales have a higher geometric resolution their radiometric accuracy – mainly with respect to originally homogeneous areas – is very low. On the contrary the coarser scales possess a better radiometric accuracy, but a lower geometric resolution. Therefore, originally homogeneous areas appear very smooth, but heterogeneous areas appear blurred. In order to decompose the image into several scales an adequate low-pass filter kernel is needed. Like the Gaussian function as probability density function of the normal

distribution – commonly used for the low-pass filtering of normally distributed data like optical images – a comparative filter window can be derived from the hyperbolic tangent distribution family introduced above (Bickle et al., 1998). The cumulative density defined as hyperbolic tangent function (cf. Section 3.2.3) leads to a corresponding probability density function given by the first derivate of the hyperbolic tangent, i.e. the squared hyperbolic secant function.

$$\frac{d \tanh(x)}{dx} = \operatorname{sech}^2(x) \quad (23)$$

The size of the belonging low-pass window can be regulated by the number of looks to be realized: the more looks the wider the window has to be chosen. Therefore, the pixel distance from the center symbolized by x is divided by the look number L . As the weighting should be symmetric with respect to the center pixel, the distance x is introduced twice. Hence, the integral from $-\infty$ to $+\infty$ approximates the look number and the resulting window definition turns out to be

$$W(x, L) = \operatorname{sech}^2\left(\frac{2x}{L}\right) = \left(\frac{2}{e^{2x/L} + e^{-2x/L}}\right)^2 = \frac{4}{e^{4x/L} + 2 + e^{-4x/L}} \quad (24)$$

Fig. 8 illustrates the slightly different behavior of the Gaussian and the hyperbolic secant square function when used as smoothing window with a shared look number of three. The sech^2 -function shows higher values for the center pixel as well as for distances wider than five pixels. Between one and four pixels the Gaussian function leads to stronger weights. This can be interpreted as follows: The sech^2 -function assigns more influence to the center pixel and the wider surrounding, while the Gaussian function focusses on the center pixel and its direct neighborhood. Therefore, single targets often appear blurred when using the Gaussian function while their size is well-preserved applying the sech^2 -window. Even point targets located in a homogeneous surrounding are well preserved by the help of the sech^2 -function although homogeneous areas are perfectly smoothed. This particular behavior is extremely important for the preservation of edges and has also been observed for the optimized edge detection in optical image data under multiple noise conditions (Deriche, 1987).

Hence, the sech^2 -function is preferred for low-pass filtering because it fits in the noise model derived above at first. And secondly, the filtered images still contain sharp edges and clear point

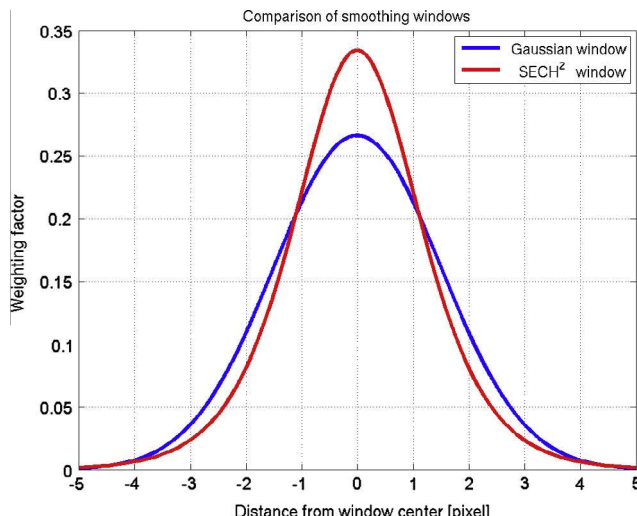


Fig. 8. Comparison of the Gaussian and the hyperbolic secant square window functions.

targets while distributed targets are sufficiently smoothed. When calculating the image pyramid, the look number is doubled for each scale layer and each direction, i.e. the finest layer is given in the original image scale, the next coarser scale encloses four looks of the finer scale. Subsampling is not performed in the current implementation – though possible in theory – in order to prevent artifacts by insufficient reconstruction routines.

3.3.2. The derivation of the look image

The core of this image enhancement technique is to find the so-called scale or look image assigning the optimal scale or look number to each pixel. The initial point is the coarsest scale with the highest radiometric accuracy. From there, the significance of the multi-scale differential Kennaugh elements is evaluated for the next finer scale. If its significance exceeds 99%, then the pixel value of the finer scale is adopted, otherwise the coarser scale is retained. As the neighboring scales are highly correlated, the decision – taken pixel-by-pixel – has to be further smoothed using the corresponding sech^2 -window. Therewith, the scale separation is assured. None of the pixel values appears twice – both in the finer and in the surrounding coarser scale – and thus, gains more weight than the others. At this point, the resulting image consequently consists of the contributions of two different scales. Comparing it to the next finer image scale, the formerly uniform look number of the coarse scale is replaced by the current look image. This procedure is repeated until the finest scale – the original image scale – is reached, i.e. the enhanced image composes out of contributions of all image scales depending on the local image content.

Fig. 9 illustrates a subset of 256 by 256 pixels of a TerraSAR-X dual-polarized HighResolutionSpotlight acquisition over the harbor area of Mannheim-Ludwigshafen in Germany geocoded to a final pixel spacing of one meter. The mono-scale pyramid layers at the left show the information content of the current scale. The scale image in the middle initiated as coarsest scale is refined with each step so that homogeneous areas still preserve the high look number of 256 and stay bright while heterogeneous areas get darker and darker indicating a lower look number and thus, a higher geometric resolution. The right column depicts the image reconstruction to the corresponding minimum look number according to the scale image in the middle column. Obviously, while the mono-scale layers in the left column gain both structures and noise with decreasing look numbers, the multi-scale images in the right column only gain structures because homogeneous areas stay perfectly smoothed thanks to the higher look number. In this sense, the scale image in the middle column could also be interpreted as texture measure – the built-up land appears darker than the open water surface – and even as edge detector because thin dark lines mark the outlines of bright objects. The interpretation of the scale image then is similar to the number of homogeneous neighboring pixels derived with other techniques (Alonso-Gonzalez et al., 2013; Ferretti et al. 2011). In contrast to the methods mentioned the scale image can directly be employed as template for smoothing further image layers like polarimetric Kennaugh elements (e.g.), see following section.

3.3.3. The image reconstruction

Now that the scale or look image is derived from the best available intensity image, it can be applied to any image layer available for the imaged landscape. The simplest application is the radiometric enhancement of multi-polarized acquisitions where the single Kennaugh elements are decomposed into a sech^2 image pyramid and subsequently interpolated by the scale image derived from the total intensity. Furthermore, it can be applied to multi-temporal images by calculating the scale image from the joint intensity and enhancing the single image layers before combining them to differential Kennaugh elements. Finally, even the multi-frequency

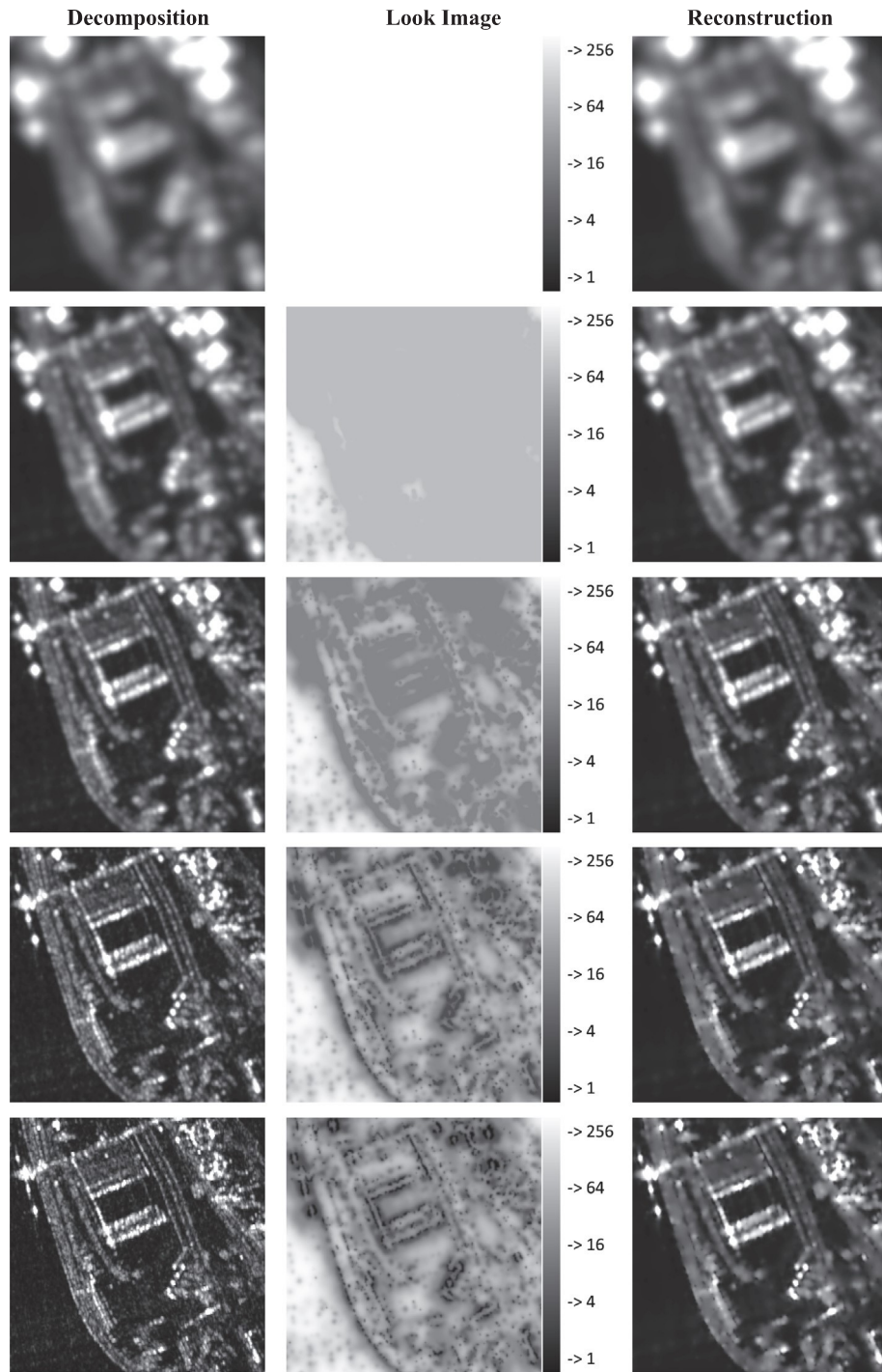


Fig. 9. The multi-scale multi-looking technique applied to a 256×256 pixel subset of a TerraSAR-X dual-polarized high resolution spotlight acquisition over the harbor area for Mannheim–Ludwigshafen in Germany. The columns show the smoothed intensity (left), the derived scale image (middle) indicating the number of looks (see gray scale), and the reconstructed multi-scale image (right) for different scales of the image pyramid represented by the corresponding look numbers in the rows.

usage is possible when interpolating a stack of multi-sensor SAR data by the help of the scale image derived from the joint total intensity. As the best available geometric resolution is preserved for the whole image stack, the multi-scale multi-looking approach can be compared to the pan-sharpening techniques which are very common in optical remote sensing.

4. Application & validation

Due to the wide range of feasible applications of this SAR image preparation framework, it is not possible to present any polariza-

tion configuration or image combination in this contribution for reasons of length. Therefore four special cases are selected and discussed in the following: (4.1) multi-temporal, multi-polarized, and multi-sensor (differential) Kennaugh elements composed of Envisat-ASAR and TerraSAR-X images for long-term monitoring including already elapsed satellite missions, (4.2) simulated hybrid-compact-pol SAR data based on a RADARSAT-2 FineQuad acquisition to show the effect of the multi-polarized and multi-scale image description and enhancement with respect to future SAR missions, (4.3) change detection by the help of differential Kennaugh elements out of two dual-co-polarized TerraSAR-X

HighResolutionSpotlight acquisitions, and finally, (4.4) the combination of polarimetric data of three wave bands (L-, C-, and X-band) acquired by three different satellites (ALOS-PALSAR, RADARSAT-2, and TerraSAR-X) in one image product, including joint image enhancement. All images cover the metropolitan region of Mannheim–Ludwigshafen in south-western Germany which is characterized by a very diversified land cover such as urban and rural settlements, forests, agricultural land, rivers, canals, natural and artificial lakes, harbors, and large industrial zones widely dominated by chemical industry.

4.1. Multi-temporal, multi-polarized and multi-sensor Kennaugh elements for long-term monitoring purposes

The first example includes images acquired by the already elapsed Envisat-ASAR satellite and the current TerraSAR-X sensor. In this manner the suitability of our approach for long-term monitoring – exceeding the lifetime of one SAR satellite mission – is proven.

4.1.1. Application

The Envisat-ASAR archive provides numerous acquisitions over one decade (2002–2012) for many sites all over the world. The presented image was acquired in dual-polarization HH and HV on 2005-07-10. The decomposed image is geocoded to a final pixel spacing of 10 m on ground which requires no initial multi-looking. The original geometric resolution is preserved as far as possible with respect to the acquisition geometry. Out of the four possible Kennaugh elements the total intensity in k_0 (Fig. 10a) and the relation between co-and cross-polarized intensity in k_1 (Fig. 10d) are selected for this study. Fig. 10 shows a subset of 120-by-120 pixels, i.e. 1.2 km by 1.2 km. For the same location a TerraSAR-X quad-pol acquisition dating from 2010-05-13 is available from which the HH and the HV channel are converted to k_0 and k_1 (see Fig. 10b and e). The geocoding to the consistent pixel size of 10-by-10 m requires an initial multi-looking using 28.64 looks to prevent aliasing effects. Obviously the TerraSAR-X image appears much sharper due to the higher geometric resolution. Even more, none of the structures apparent in the TerraSAR-X images can be relocated in

the Envisat-ASAR images so that visual comparison is nearly impossible. The differential Kennaugh elements including joint multi-scale multi-looking image enhancement are given in Fig. 10c and f with the joint intensity image in the background. Only changes of more than 10 dB are colored – red for positive change and blue for negative change –, changes of less than 10 dB are transparent.

4.1.2. Validation

It is interesting to see that the enhanced differential Kennaugh elements in Fig. 10c and f clearly delineate single features despite the high discrepancy in the geometric resolution. Furthermore, thanks to the separation of intensity and polarimetry, the two Kennaugh elements show completely independent information. A change in the intensity (Fig. 10c) is not necessarily connected to a change in polarimetry (Fig. 10f) and the other way round. The enhanced intensity image in the background combined out of both input images transfers the high geometric resolution of TerraSAR-X to the Envisat-ASAR images. Structures that are not necessarily apparent in the single image now are amplified. All changes detected can be referred to human activities as they mainly appear in built-up areas in the right part of the image. On the left, agricultural land use back in 2005 has turned to industry in 2010. The rectangular structures are known from a detailed survey reported by Schmitt et al. (2014) to belong to a factory building erected from 2008 until 2010. The single red dots in the left upper part of Fig. 10c indicate a new installed electric power line. Naturally, the differing frequency and image resolution have a strong impact on the image comparison. Anyway, this example proves that a thoroughly data preparation still enables the detection of distinct anthropogenic changes over long periods of time.

4.2. Multi-scale and multi-polarized Kennaugh elements for future SAR satellite missions

The second example underlines the flexibility of the Kennaugh descriptor with respect to future SAR missions as well as the impact of the multi-scale image enhancement in comparison to a constant look number.

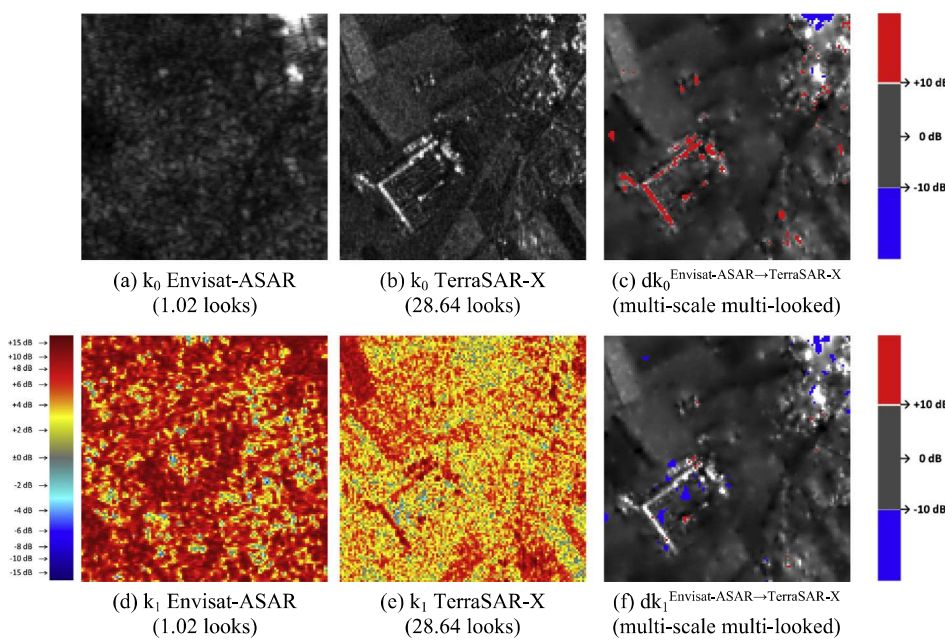


Fig. 10. Multi-temporal Kennaugh elements combined of an Envisat-ASAR acquisition in HH–HV polarization on 2005-07-10 and the HH–HV channels of a TerraSAR-X quad-pol acquisition on 2010-05-13 showing anthropogenic changes such as a factory building and an electric power line constructed in the meantime.

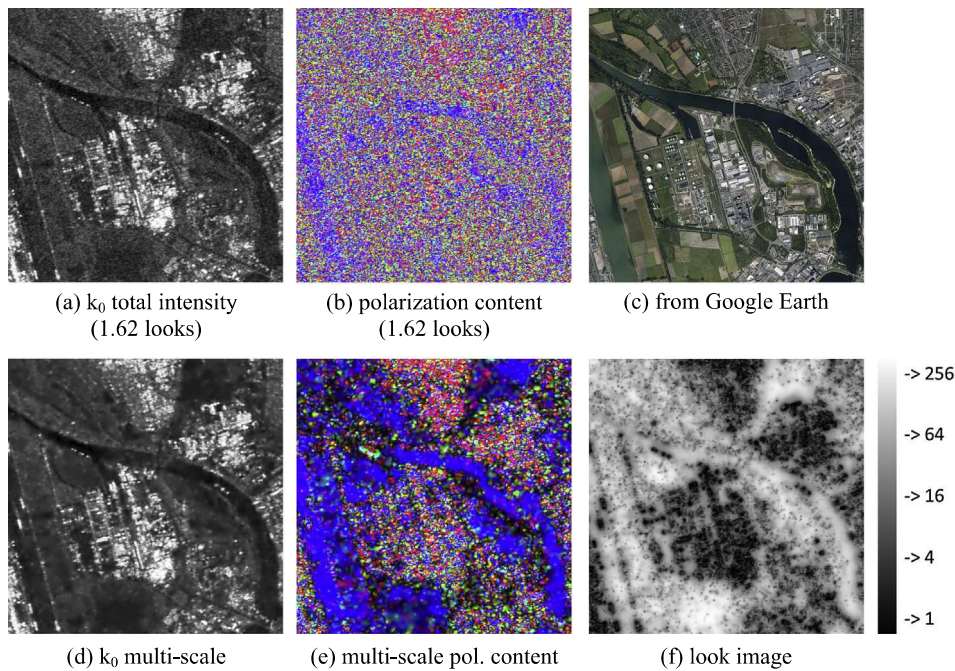


Fig. 11. Simulated hybrid-compact-pol data based on a RADARSAT-2 FineQuad scene acquired on 2009-08-16 (minimal look number: 1.62): the effect of varying look numbers on intensity and polarization.

4.2.1. Application

The single look complex data of a RADARSAT-2 FineQuad scene dating from 2009-08-16 is delivered with a pixel spacing of approximately five meters in slant range geometry. Considering the mean incidence angle of about 23 degrees the image is smoothed using a minimum look number of 1.62 for the sech^2 -window. Hence, information loss during the geocoding of the decomposed image data to a 6.25 by 6.25 m pixel raster on ground is prohibited. The decomposition includes the simulation of hybrid-compact-pol data and results in the Kennaugh elements k_0 , k_3 , k_5 , and k_8 . Fig. 11c gives an overview of the test site which composes of fine structured industrial areas, more or less thin canals, and relatively homogeneous agricultural land. The total intensity (a subset of 512 by 512 pixels) represented by k_0 is depicted in Fig. 11 with a uniform look number (Fig. 11a) and with varying look number according to the multi-scale multi-looking approach respectively (Fig. 11d). Additionally, the scale image shown in Fig. 11f is produced. The scale and therewith the look number varies with the homogeneity of the landscape. Thus, homogeneous regions like fields or open water appear bright indicating high look numbers or a high number of homogeneous neighboring pixels (cf. Alonso-Gonzalez et al., 2013 or Ferretti et al., 2011). Industrial areas are characterized by numerous black dots standing for low look numbers and therefore maximum geometric resolution.

4.2.2. Validation

Comparing Fig. 11b–e that illustrate the polarization content (Red: $P_{\text{retardance}}$, Green: $P_{\text{diattenuation}}$, Blue: $P_{\text{absorption}}$) the advantage of the multi-scale multi-looking approach becomes evident. While the polarization content using a uniform number of looks (Fig. 11b) does not reveal any interpretable structure, the polarization content after multi-scale multi-looking shows smooth bluish areas characterized by high deviations in the absorption element (Fig. 11e). In contrast to that, highly structured areas indicate a diversity of the polarization contents. Therefore, Fig. 12 illustrates the single Kennaugh elements derived from the simulated

hybrid-compact-polarized data. Only deviations whose significance exceeds 99% are marked in colors, all others are made transparent so that the underlying intensity image shines through. For all three elements the significant polarimetric information is restricted to man-made objects like industrial buildings or vessels using a constant look number, see Fig. 12a–c. Natural or distributed targets only show minor polarimetric information content. In the multi-scale representation in Fig. 12d–f the Kennaugh element k_3 marks large homogeneous areas that appear bluish which can be referred to surface scattering over smooth fields and open water surfaces (Fig. 12d). Regarding k_5 and k_8 , obviously the portion of significant polarimetric information is increased. In addition to that, not only red (positive) or blue (negative), but much more different shades can be perceived both over industrial areas and over natural targets. In conclusion, the multi-scale multi-looking image enhancement enables the polarimetric description of distributed targets by increasing the look number. But, it simultaneously preserves the polarimetric behavior of deterministic targets. As the maximum geometric resolution is assured over heterogeneous regions deterministic targets still appear sharp.

4.3. Multi-temporal, multi-scale, and multi-polarized Kennaugh elements

In this section the multi-temporal aspect of this novel technique is highlighted again, i.e. the differential Kennaugh elements are directly utilized for change detection and change characterization. For validation purposes, the results of former studies comparing this approach to visually derived reference data are cited.

4.3.1. Application

For the highly structured harbor zone depicted in Fig. 13a subsets (1024 by 1024 pixels) of two TerraSAR-X HighResolutionSpotlight scenes in dual-co-polarization (HH & VV) dating from (a) 2008-09-21 and (b) 2008-10-02 are combined to differential Kennaugh elements. In order to gain best geometric resolution a final pixel spacing of one meter on ground is chosen which corresponds

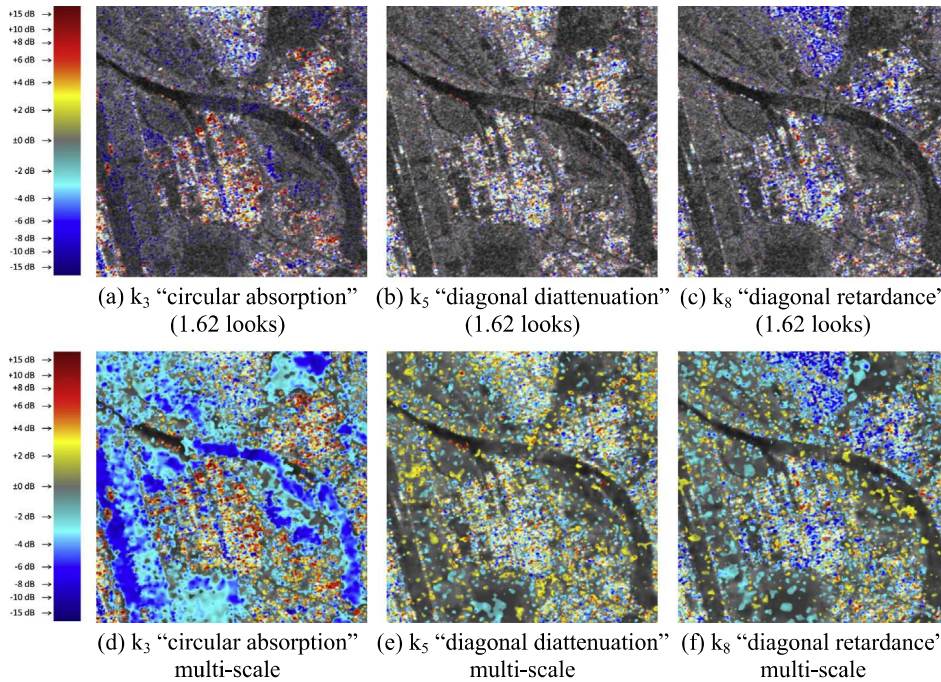


Fig. 12. Simulated hybrid-compact-pol data based on a RADARSAT-2 FineQuad scene: the partial-polarimetric channels with and without multi-scale multi-looking, only significant contributions (>99%) are colored (yellow to red for positive values, turquoise to blue for negative values). (For interpretation of the references to color in this figure legend, the reader is referred to the web version of this article.)

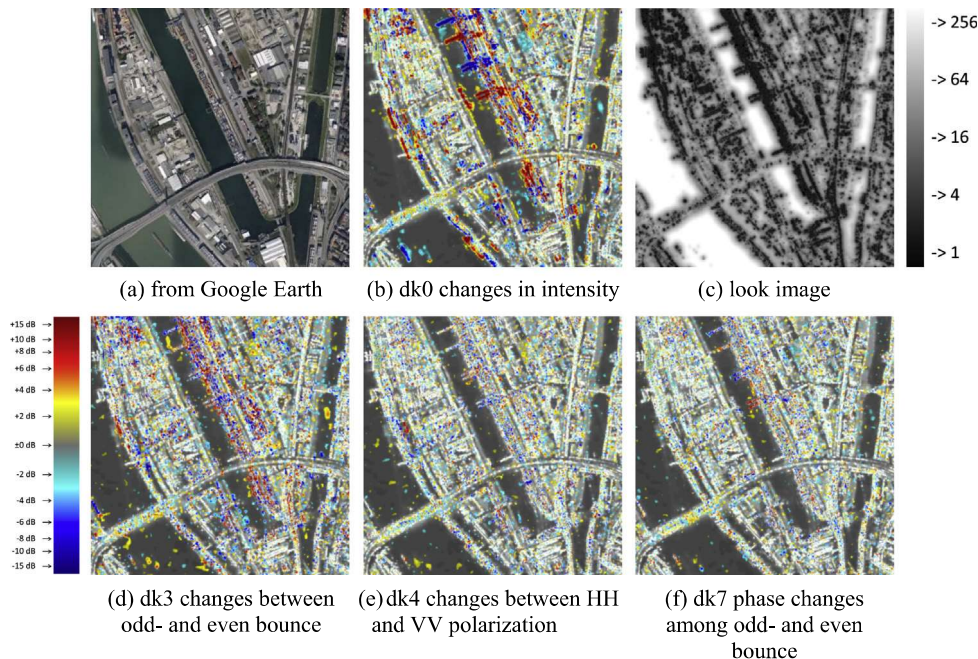


Fig. 13. Optical image and differential Kennaugh elements from two dual-co-polarized TerraSAR-X HighResolutionSpotlight scenes, positive changes in red, negative changes in blue, negligible changes are transparent with the joint intensity image in the background. (For interpretation of the references to color in this figure legend, the reader is referred to the web version of this article.)

to 0.66 looks, i.e. the image is slightly oversampled. Despite that, the multi-scale multi-looking approach enables the reliable detection of changes in the polarimetric backscattering by introducing radiometric stability. The look image derived from the joint intensity is given in Fig. 13c. It clearly delineates bright homogeneous areas that indicate open water, dark heterogeneous areas that mark industrial facilities, and shades of grey for areas with medium texture over all standing for bare soil.

4.3.2. Validation

The intensity changes shown in Fig. 13b can easily be referred to objects moved from one location to another in-between the two acquisitions like ships, cranes, and containers whereat red stands for the appearance of an object – i.e. its new location – and blue stands for its disappearance – i.e. its former location. As SAR inherent noise is almost completely removed, the differential Kennaugh element values whose significance exceeds 99% (see blue and red

colors in Fig. 13b) can directly interpreted as detected changes. Former studies even proved the reliability of this change detection method in contrast to human interpreters. The changes detected by differential Kennaugh elements achieved an overall accuracy of more than 96% which is much more than the inner concordance of the five human interpreters involved (Schmitt, 2012). In contrast to common change detectors that derive one change measure from the combination of all channels (Marino et al., 2013 e.g.), our approach describes the change of each Kennaugh element separately. And it is most interesting to see, that each of these polarimetric differential Kennaugh elements in Fig. 13d–f seems to behave completely independent from the changes in the total intensity (Fig. 13b). Indeed, the theory of differential Kennaugh elements determines this independence. In this example, however, the majority of changes in polarimetric Kennaugh elements correspond to changes in the total intensity in size and location anyway because both changes originate from the same target change on ground. With respect to applications in agriculture this separation of intensity from polarimetry is very beneficial because changes of soil moisture only affect the back-scattered intensity while changes in the scattering mechanism – e.g. by plant growth – result in a different polarimetric behavior (Leichtle, 2013). The meaning of the polarimetric changes or in other words their correlation to changes on ground still is subject to recent studies. Anyways, this example accounts for the increased information content of multi-polarized SAR data on the one hand and for the advantageous description of multi-temporal and multi-polarized SAR data by normalized multi-scale (differential) Kennaugh elements – even replacing conventional change detection – on the other hand.

4.4. Multi-frequency, multi-scale, and multi-polarized Kennaugh elements

The last example focusses on the combination and joint enhancement of multi-frequency polarimetric SAR data acquired by different satellite sensors, thus a multi-sensor combination. In

order to underline the benefit of this novel approach the multi-frequency images are faced with multi-frequency combinations of standard polarimetric decompositions.

4.4.1. Application

As today's satellite sensors are limited to one single wave band, multi-frequency SAR images must be combined out of the contributions of different satellite sensors. In this example the L-band measurement comes from ALOS-PALSAR (2007-04-17), the C-band measurement is performed by RADARSAT-2 (2009-04-18), and the X-band image is acquired by TerraSAR-X (2010-04-21). All measurements comprise all four polarizations, i.e. quad-pol data. Though acquired in several years all images date from mid-April so that seasonal changes should become negligible. Fig. 14a–c depicts the total intensity in k_0 of the three polarimetric images. It is obvious that there is a high discrepancy in the geometric resolution which leads to a very different level of detail and consequently to a high variation in the look numbers needed to generate the combined image with a raster size of 10 by 10 m on ground: three looks in L-band – required to produce square resolution cells, but still oversampled – (Fig. 14a), around two looks in C-band (Fig. 14b), and approximately twenty-nine looks in X-band (Fig. 14c). The optical image in Fig. 13d gives an impression of the imaged landscape. Due to the lower geometric resolution a subset of 256 by 256 pixels with widely homogeneous areas like fields or open water, and just one settlement with residential houses exclusively is chosen. The following two images illustrate the combination of the three intensity layers according to their wave length: Red for L-band, Green for C-band, and Blue for X-band. In Fig. 14e the look numbers are constant all over the image, which leads to blurred structures in L-band, very noisy fields in C-band, but sharp features in X-band because of the very high variation in the number of looks. The scale image is derived from the combined intensity image incorporating around thirty-four looks. Applying this scale image to the single Kennaugh layers produces a very smooth, but detail-preserving image as shown in Fig. 14f. In doing so, the high geometric resolution of TerraSAR-X is

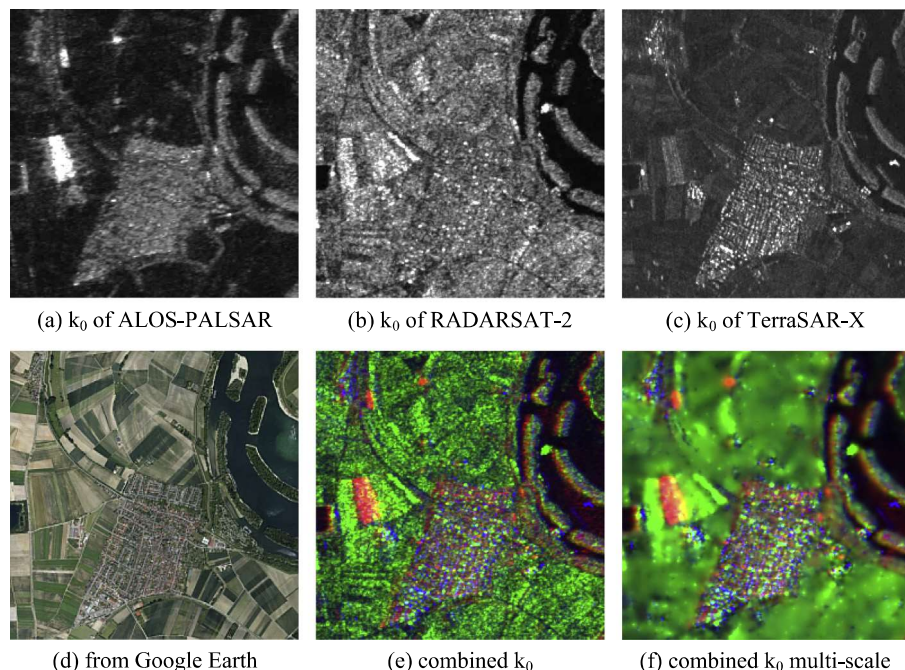


Fig. 14. Optical image, multi-frequency intensities and combinations of these from fully polarimetric ALOS-PALSAR, RADARSAT-2, and TerraSAR-X scenes, color coded according to the wave band (R: L-band, G: C-band, B: X-band).

assigned to the images of RADARSAT-2 and ALOS-PALSAR. Hence, the multi-scale multi-looking acts like the pan-sharpening technique very common to optical remote sensing where the higher geometric resolution of the pan-chromatic channel is used to sharpen the measurements of the remaining spectral channels.

4.4.2. Validation

The multi-spectral combination of image intensities is well-known from optical remote sensing. Thus, k_0 representing nothing else than simple intensity values can easily be combined to a multi-spectral image, see Fig. 14f. Regarding the polarimetric information content, the question arises whether the single output layers can also be combined to meaningful multi-spectral images. Or in other words: Do polarimetric decompositions deliver comparable results even for varying spectral bands? Three different decomposition techniques are listed in Fig. 15: the Cloude–Pottier decomposition consisting of entropy, anisotropy, and mean alpha angle (Cloude and Pottier, 1996), the Freeman–Durden decomposition into surface, double-bounce, and volume intensities (Freeman and Durden, 1998), and the polarization content of the Kennaugh elements according to their orientation parallel, diagonal, and circular.

Obviously the Cloude-Pottier decomposition (Fig. 15a–c) does not allow for the inter-frequency comparison. The colors indicate that mainly L-band (red) and X-band (blue) show much higher values in entropy (Fig. 15a) and mean alpha angle (Fig. 15c) than C-band. Quite the contrary, C-band (green) dominates the anisotropy (Fig. 15b). The high entropy (Fig. 15a) with TerraSAR-X probably

results from the well-known significant crosstalk between co- and cross-polar channels. RADARSAT-2 in contrast is characterized by a very low noise floor and very good inter-channel signal separation leading to lower entropy values. The high entropy in the ALOS-PALSAR image mainly over bare surfaces might be an effect of a low signal to noise ratio. The characteristics of the mean alpha angle (Fig. 15c) can presumably be referred to the discrepancies in the entropy layers.

With respect to the Freeman-Durden decomposition RADARSAT-2 obviously delivers higher surface scattering values (Fig. 15e) over agricultural land than the others. On the one hand, this effect comes from the wavelength of the sensor, which is optimized for crop monitoring. But, on the other hand, this again could be an effect of the very low noise floor with RADARSAT-2 quad-pol images. The distribution of double-bounce targets naturally varies with wavelength and image resolution. Therefore, the dots in Fig. 15d are even red, blue, or green, but almost nothing in-between. In some cases the discrepancies of the multi-temporal acquisitions might also be referred to changes in the landscape. Though seasonal changes are negligible (same month for all acquisitions) a change in the land use in-between the time series from 2007 until 2010 will also affect the polarimetric behavior. However, the Kennaugh element descriptor is able to deliver at least three clearly structured multi-frequency images in Fig. 15g-i describing the oriented polarization content. Thanks to the joint image enhancement via the multi-scale multi-looking approach the polarimetric relations are treated equally throughout all

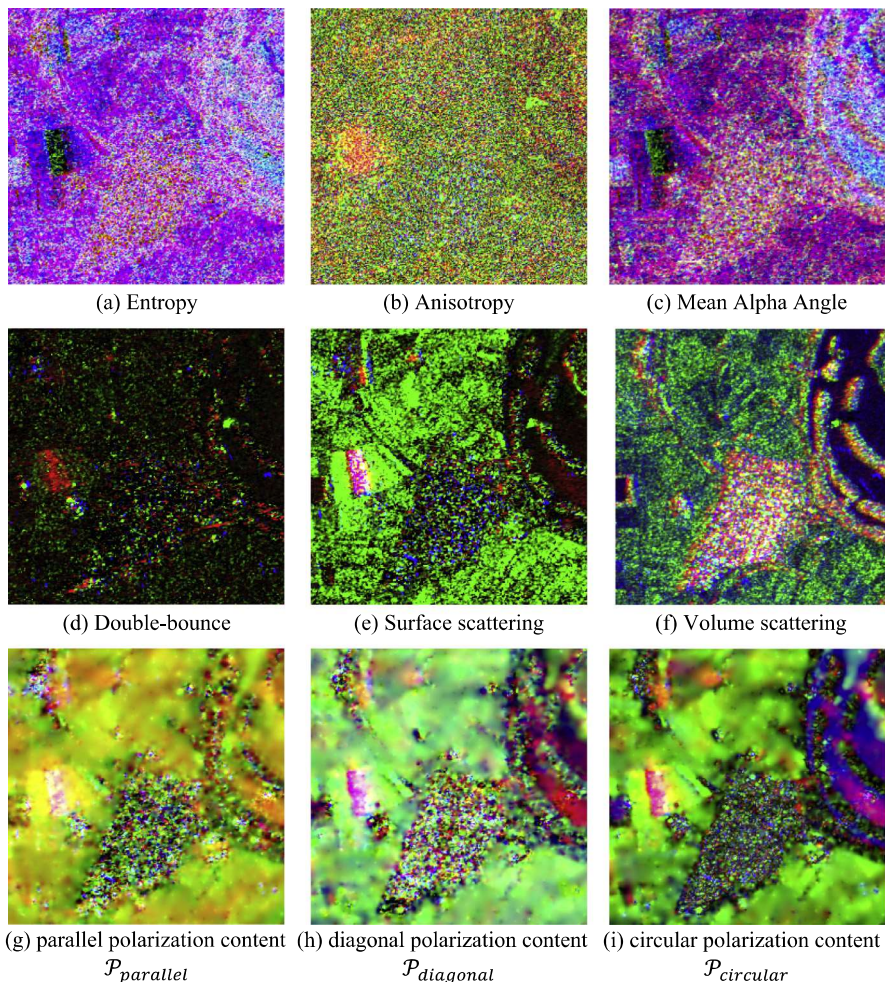


Fig. 15. Three multi-frequent polarimetric decompositions: Claude-Pottier (first row), Freeman-Durden (second row), polarization content of Kennaugh elements by orientation (third row) color coded according to R: L-band (ALOS-PALSAR), G: C-band (RADARSAT-2), B: X-band (TerraSAR-X).

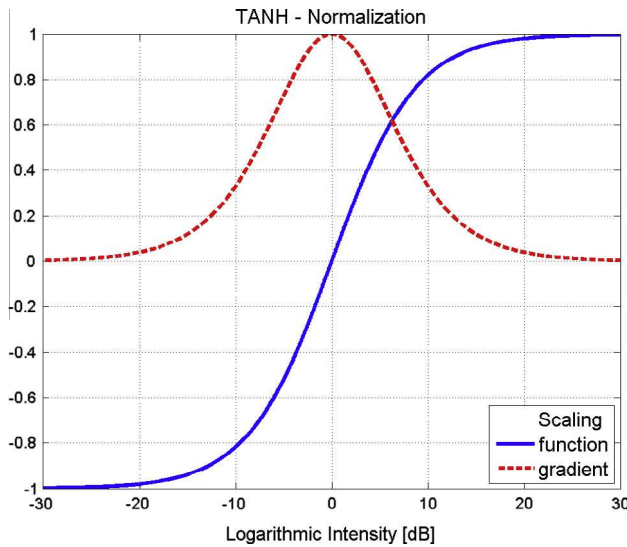


Fig. 16. The hyperbolic tangent function and its gradient by the logarithmic intensity and logarithmic intensity quotients respectively.

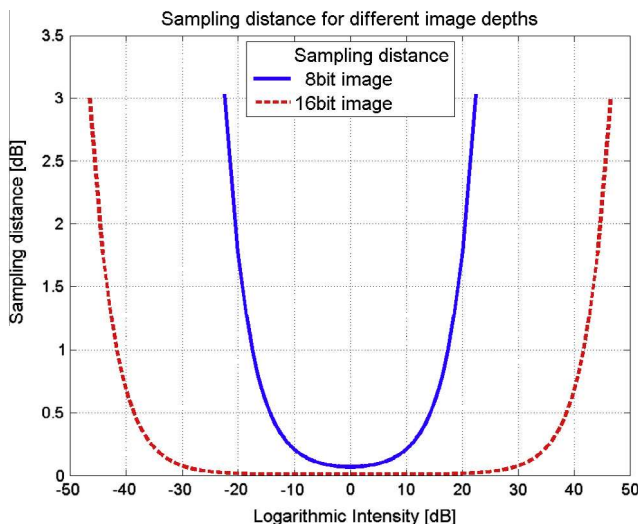


Fig. 17. The sampling distances for integer images at different bit depths of 8 and 16 when using the hyperbolic tangent normalization and Eqs. (A2) & (A3) by their logarithmic intensity values.

multi-frequent contributions. Keeping in mind that the influence of the image intensity has already been removed for normalized Kennaugh elements, these images show the pure polarimetric information content. Additionally, the sign of the Kennaugh elements being removed in the polarization content – mainly for display reasons in this example – might hold much more information than presentable in this short overview. In a nutshell, the Kennaugh framework provides a comparable and robust representation of multi-polarized SAR data independent of sensor or wavelength. It includes joint image enhancement and thus, guarantees the preservation of image information.

5. Conclusion

The intention of this paper is to introduce a novel very versatile SAR image preparation technique based on Kennaugh elements. It is applicable to all kind of multi-scale, multi-polarized, multi-temporal, multi-frequent, and thus, multi-sensor SAR data. In combination with the multi-scale-multi-looking approach which

deduces the optimal look factor from the best available SAR intensity image, a pan-sharpening like image enhancement is realized. It guarantees smooth homogeneous areas, very detailed heterogeneous areas, and last but not least uniform smoothing over all image channels. This careful data handling enables an extremely sensitive technique to highlight polarimetric backscattering behavior as well as temporal or even spectral variations. The significance of the information can be estimated via the perturbation-based noise model which is especially suited for the stochastic description of Kennaugh elements. Although this might induce some problems regarding natural objects with low backscattering intensity, it is essential for target detection in highly structured environments and change detection in general. Out of the wide range of conceivable applications only four simple examples underlining the effectiveness of this technique in terms of data quality are shown here. The examples prove that this approach excels most notably in urban applications being the only polarimetric approach that guarantees both high geometric resolution and radiometric stability at the same time. Hence, image data from any current or former SAR satellite mission can be handled by this approach and delivered in a consistent framework. With respect to new SAR missions like TanDEM-X, the RADARSAT-Constellation, or maybe TanDEM-L the aim is to further include interferometric measurements in order to generate highly accurate and up-to-date elevation models to support the geocoding and calibration process.

Acknowledgements

Thanks to ESA, JAXA, MDA, and DLR for providing the image data.

ALOS-PALSAR data ©JAXA, 2007.

RADARSAT-2 Data and Product © MDA (2009) – All Rights Reserved.

TerraSAR-X data ©DLR, 2008 and 2010.

ENVISAT-ASAR data ©ESA, 2005.

Appendix A

A.1. The hyperbolic tangent

Two definitions for the hyperbolic tangent function are used in this paper:

$$\tanh x = \frac{e^{2x} - 1}{e^{2x} + 1} = \frac{e^x - e^{-x}}{e^x + e^{-x}} \quad (\text{A1})$$

An advantage of this function is its closed value range given by $\lim_{x \rightarrow \infty} \tanh x = 1$ and $\lim_{x \rightarrow -\infty} \tanh x = -1$. Fig. 16 draws the function as well as its first derivate in order to visualize its sensitivity which is maximal around zero and falls down towards infinity.

A.2. Efficient archiving of TANH normalized values

For efficient archiving or data exchange integer values are generally preferred because of the minor file size. Assuming an arbitrary image depth ϑ , normalized Kennaugh variables can easily be transferred to unsigned integer values and vice versa as follows:

$$DN(k_i) = k_i \cdot (2^{\vartheta-1} - 1) + 2^{\vartheta-1} \quad (\text{A2})$$

$$k_i(DN) = DN \cdot (2^{\vartheta-1} - 1)^{-1} - \frac{2^{\vartheta-1}}{2^{\vartheta-1} - 1} \quad (\text{A3})$$

As mostly 8 bit and 16 bit images are utilized in practice Fig. 17 shows the corresponding sampling rates. Maximum sampling rates are achieved around zero with values of 0.07 dB (8 bit) and 0.0003 dB (16 bit). The sampling rates reduce towards the edges

of the value range reaching their minimum sampling with 3 dB in both cases. The maximum representable absolute values are 24 dB (8 bit) and 48 dB (16 bit). In short, for 8 bit data all values in the range of ± 17.5 dB are sampled with a distance below 1 dB, for 16 bit data this range is extended to ± 41.7 dB which is far enough with respect to today's SAR sensors.

A.3. Look numbers of combined intensities

The look number may alternatively be defined as the reduction of the variance: $L = \frac{\sigma^2}{\sigma_L^2}$. Starting with the intensity defined as mean of two intensities with varying look numbers $I = \frac{I_a + I_b}{2}$ the variance propagation leads to: $\sigma_L^2 = \left(\frac{\partial I}{\partial I_a}\right)^2 \cdot \sigma_a^2 + \left(\frac{\partial I}{\partial I_b}\right)^2 \cdot \sigma_b^2 = \frac{1}{4} \cdot \frac{\sigma^2}{n} + \frac{1}{4} \cdot \frac{\sigma^2}{m} = \frac{1}{4} \cdot \frac{1}{n+m} \cdot \sigma^2$ whereas the partial derivations unfold to: $\frac{\partial I}{\partial I_a} = \frac{\partial I}{\partial I_b} = \frac{1}{2}$. The reduction of the variance can now be inverted in order to get the look number of the combined intensity as follows:

$$L = \frac{\sigma^2}{\sigma_L^2} = \frac{4}{\frac{1}{n} + \frac{1}{m}} \quad (\text{A4})$$

Thus, the look number of the combined intensity equals the doubled harmonic mean of the look numbers of the input intensities.

A.4. Difference of correlated intensities

The look numbers of the two multi-scale intensities shall be given by n and m whereas n is the look number of the coarser scale and thus, $1 \leq m \leq n$. The input intensities can be described as mean of n and m single intensities respectively. Sharing the same location, the intensity values from 1 to m appear twice, so the difference of two independent intensities \bar{I}_a and \bar{I}_b is scaled by a factor composed of the two look numbers as given in the following:

$$\begin{aligned} I_{\text{coarse}} - I_{\text{fine}} &= \frac{1}{n} \sum_{i=1}^n I_i - \frac{1}{m} \sum_{i=1}^m I_i = \left\{ \frac{1}{n} \sum_{i=1}^m I_i + \frac{1}{n} \sum_{i=m+1}^n I_i \right\} - \frac{1}{m} \sum_{i=1}^m I_i \\ &= \frac{1}{n} \sum_{i=m+1}^n I_i - \left\{ \frac{1}{m} \sum_{i=1}^m I_i - \frac{1}{n} \sum_{i=1}^m I_i \right\} = \frac{1}{n} \sum_{i=m+1}^n I_i - \left\{ \frac{1}{m} - \frac{1}{n} \right\} \cdot \sum_{i=1}^m I_i \\ &= \frac{1}{n} \sum_{i=m+1}^n I_i - \frac{n-m}{n-m} \sum_{i=1}^m I_i = \frac{n-m}{n} \cdot \bar{I}_a - \frac{n-m}{n} \cdot \bar{I}_b = \frac{n-m}{n} \cdot \{\bar{I}_a - \bar{I}_b\} \\ \bar{I}_a - \bar{I}_b &= \frac{n}{n-m} \cdot \{I_{\text{coarse}} - I_{\text{fine}}\} \end{aligned} \quad (\text{A5})$$

A.5. Sum of correlated intensities

A similar problem occurs when summing up the input values. As the values of the finer scale appear twice, but with different weights, the intensity of the finer scale has to be scaled by a weighting factor p . In order to obtain the same uncorrelated intensities as derived for the difference, factor p has to be defined as follows:

$$\begin{aligned} I_{\text{coarse}} + I_{\text{fine}} &= \frac{1}{n} \sum_{i=1}^n I_i + \frac{p}{m} \sum_{i=1}^m I_i = \left\{ \frac{1}{n} \sum_{i=1}^m I_i + \frac{1}{n} \sum_{i=m+1}^n I_i \right\} + \frac{p}{m} \sum_{i=1}^m I_i \\ &= \frac{1}{n} \sum_{i=m+1}^n I_i + \left\{ \frac{p}{m} \sum_{i=1}^m I_i + \frac{1}{n} \sum_{i=1}^m I_i \right\} = \frac{1}{n} \sum_{i=m+1}^n I_i + \left\{ \frac{p}{m} + \frac{1}{n} \right\} \cdot \sum_{i=1}^m I_i \\ &= \frac{1}{n} \sum_{i=m+1}^n I_i + \frac{n-p+m}{n-m} \cdot \sum_{i=1}^m I_i = \frac{n-m}{n} \cdot \bar{I}_a + \frac{n-p+m}{n} \cdot \bar{I}_b = \frac{n-m}{n} \cdot \{\bar{I}_a + \bar{I}_b\} \\ \rightarrow p &= \frac{n-2m}{n} = 1 - 2 \cdot \frac{m}{n} \end{aligned} \quad (\text{A6})$$

When the proportionality factor $\frac{n}{n-m}$ known from the difference of correlated intensities (see Eq. (A5)) is applied additionally, even

the sum of two correlated intensities can be converted to the sum of two uncorrelated intensities, as follows:

$$\bar{I}_a + \bar{I}_b = \frac{n}{n-m} \cdot \left\{ I_{\text{coarse}} + \left(1 - 2 \cdot \frac{m}{n}\right) \cdot I_{\text{fine}} \right\} \quad (\text{A7})$$

Thus, combining Eqs. (A5) and (A7) enables the generation of an unbiased differential Kennaugh element as given in Eq. (14).

References

- Adelson, E.H., Anderson, C.H., Bergen, J.R., Burt, P.J., Ogden, J.M., 1984. Pyramid methods in image processing. *RCA Engineer* 29 (6), 33–41.
- Alberga, V., 2004. Comparison of polarimetric methods in image classification and SAR interferometry applications. PhD thesis. Technical University of Chemnitz, Germany.
- Alonso-González, A. et al., 2013. Bilateral distance based filtering for polarimetric SAR data. *Remote Sensing* 5 (11), 5620–5641. <http://dx.doi.org/10.3390/rs5115620>.
- Alonso-González, A., López-Martínez, C., Salembier, P., 2014. PolSAR Time series processing with binary partition trees. *IEEE Trans. Geosci. Remote Sens.* 34 (6), 3553–3567.
- Anderson, D.G.M., Barakat, R., 1994. Necessary and sufficient conditions for a Mueller matrix to be derivable from Jones matrix. *J. Opt. Soc. Am. A* 11 (8), 2305–2319.
- Bamler, R., Hartl, P., 1998. Synthetic aperture radar interferometry. *Inverse Prob.* 14, 1–54.
- Bickle, T., Lakatos, B.G., Mihálykó, C., Ulbert, Z., 1998. The hyperbolic tangent distribution family. *Powder Technol.* 97, 100–108.
- Boerner, W.-M., 2010. PolSARPro v3.0-Lecture Notes, Basic Concepts in Radar Polarimetry, <http://earth.eo.esa.int/polsarpro/Manuals/LN_Basic_Concepts.pdf> (last access 17.02.14).
- Boulvert, F., Le Brun, G., Le Jeune, B., Cariou, J., Martin, L., 2009. Decomposition algorithm of an experimental Mueller matrix. *Opt. Commun.* 282, 692–704.
- Bouyahiaa, Z., Benyoussef, L., Derrode, S., 2008. Change detection in synthetic aperture radar images with a sliding hidden Markov chain model. *J. Appl. Remote Sens.*
- Bovolo, F., Bruzzone, L., 2005. A detail-preserving scale-driven approach to change detection in multitemporal SAR images. *IEEE Trans. Geosci. Remote Sens.* 43 (12), 2963–2972.
- Brisco, B., Schmitt, A., Murnaghan, K., Kaya, S., Roth, A., 2011. SAR polarimetric change detection for flooded vegetation. *Int. J. Digital Earth* 6 (2), 103–114.
- Cameron, W.L., Youssef, N.N., Leung, L.K., 1996. Simulated polarimetric signatures of primitive geometrical shapes. *IEEE Trans. Geosci. Remote Sens.* 34 (3), 793–803.
- Carinotte, C., Derrode, S., Bourennane, S., 2006. Unsupervised change detection on SAR images using fuzzy hidden markov chains. *IEEE Trans. Geosci. Remote Sens.* 44 (2), 432–441.
- Castleman, K.R., 1996. *Digital Image Processing. Signal Processing*, second ed. Prentice-Hall.
- Charbonneau, F.J., Brisco, B., Raney, R.K., McNairn, H., Liu, C., Vachon, P.W., Shang, J., DeAbreu, R., Champagne, C., Merzouki, A., Gelsetzer, T., 2010. Compact polarimetry overview and applications assessment. *Can. J. Remote Sens.* 36 (2), 298–315.
- Cheng, J., Berger, T., 2003. On the difference of two sums of independent generalized gamma random variables with applications to error performance analysis and outage probability evaluation. In: Proc. ISIT 2003, Yokohama, Japan.
- Cloude, S.R., 2006. POL-INSAR Training Course. <http://earth.eo.esa.int/polsarpro/Manuals/I_Pol-InSAR_Training_Course.pdf> (last access 2014-02-17).
- Cloude, S.R., 2009. *Polarisation – Applications in Remote Sensing*. Oxford University Press.
- Cloude, S.R., Pottier, E., 1996. A review of target decomposition theorems in radar polarimetry. *IEEE Trans. Geosci. Remote Sens.* 34 (2), 498–518.
- Cloude, S.R., Pottier, E., 1997. An entropy based classification scheme for land applications of polarimetric SAR. *IEEE Trans. Geosci. Remote Sens.* 35 (1), 68–78.
- Conradsen, K., Nielsen, A.A., Schou, J., Skriver, H., 2003. A test statistic in the complex Wishart distribution and its application to change detection in polarimetric SAR data. *IEEE Trans. Geosci. Remote Sens.* 41 (1), 4–19.
- Deriche, R., 1987. Using Canny's criteria to derive a recursively implemented optimal edge detector. *Int. J. Comput. Vision*, 167–187.
- Elachi, C., 1988. *Spaceborne Radar Remote Sensing: Applications and Techniques*. IEEE Press, New York.
- Erten, E., Reigber, A., Ferro-Famil, L., Hellwich, O., 2012. A new coherent similarity measure for temporal multichannel scene characterization. *IEEE Trans. Geosci. Remote Sens.* 50 (7), 2839–2851.
- Espinosa-Luna, R., Rodríguez-Carrera, D., Bernabeua, E., Hinojosa-Ruiz, S., 2008. Transformation matrices for the Mueller-Jones formalism. *Sci. Direct Optik* 119, 757–765.
- Ferretti, A., Prati, C., Rocca, F., 2001. Permanent scatterers in SAR interferometry. *IEEE Trans. Geosci. Remote Sens.* 39 (1), 8–20.
- Ferretti, A. et al., 2011. A new algorithm for processing interferometric data-stacks: SqueezSAR. *IEEE Trans. Geosci. Remote Sens.* 49 (9), 3460–3470.
- Freeman, A., Durden, S.L., 1998. A three-component scattering model for polarimetric SAR data. *IEEE Trans. Geosci. Remote Sens.* 36 (3), 963–973.

- Goodman, J.W., 1976. Some fundamental properties of speckle. *J. Opt. Soc. Am.* 66 (11), 1145–1150.
- Hanssen, R.F., 2001. Radar Interferometry: Data Interpretation and Error Analysis. Kluwer Academic Publishers, Dordrecht, The Netherlands.
- Hong, S.-H., Wdowinski, S., 2013. Double-bounce component in cross-polarimetric SAR from a new scattering target decomposition. *IEEE Trans. Geosci. Remote Sens.*
- Huber, M., Hummelbrunner, W., Raggam, J., Small D., Kosmann, D., 2004. Technical aspects of Envisat-ASAR geocoding capability at DLR. In: Proc. of ENVISAT and ERS Symposium, Salzburg, Austria.
- Huynen, J.R., 1970. Phenomenological theory of Radar targets. PhD thesis. Technical University of Delft, The Netherlands.
- Kerwien, N., 2007. On the Influence of Polarization Effects in the Microscopic Image Generation (Language: German, original title: Zum Einfluss von Polarisationseffekten in der mikroskopischen Bildentstehung). University of Stuttgart, Germany.
- Le Roy-Bréhonet, F., Le Jeune, B., Eliès, P., Cariou, J., Lotrian, J., 1996. Optical media and target characterization by Mueller matrix decomposition. *J. Phys. D Appl. Phys.* 29, 34–38.
- Lee, J.-S., Pottier, E., 2009. Polarimetric Radar Imaging – from Basics to Applications. CRC Press Taylor&Francis Group, Boca Raton.
- Lee, J.S., Jurkevich, L., Dewaele, P., Wambacq, P., Oosterlinck, A., 1994. Speckle filtering of synthetic aperture radar images: a review. *Remote Sens. Rev.* 8, 313–340.
- Lee, J.-S., Grunes, M.R., Ainsworth, T.L., Du, L.-J., Schuler, D.L., Cloude, S.R., 1999. Unsupervised classification using polarimetric decomposition and the complex Wishart classifier. *IEEE Trans. Geosci. Remote Sens.* 37 (5), 2249–2258.
- Leichtle, T., 2013. Crop Classification based on multi-polarized, multi-temporal and multi-frequency RADARSAT-2 and TerraSAR-X Data for the RAMSAR site upper rhine. Master thesis. Technical University of Graz, Austria. <https://online.tugraz.at/tug_online/wbAbs.showThesis?pThesisNr=51344&pOrgNr=13071#>.
- Liao, M., Jiang, L., Lin, H., Huang, B., Gong, J., 2008. Urban change detection based on coherence and intensity characteristics of SAR imagery. *Photogr. Eng. Remote Sens.* 74 (8), 999–1006.
- López-Martínez, C., Fàbregas, X., 2008. Model-based polarimetric SAR speckle filter. *IEEE Trans. Geosci. Remote Sens.* 46 (11), 3894–3907.
- Lopez-Sanchez, J.M., Cloude, S.R., Ballester-Berman, J.D., 2012. Rice phenology monitoring by means of SAR polarimetry at X-band. *IEEE Trans. Geosci. Remote Sens.* 50 (7), 2695–2709.
- Lu, S.-Y., Chipman, R.A., 1996. Interpretation of Mueller matrices based on polar decomposition. *J. Opt. Soc. Am. A* 13 (5), 1106–1113.
- Marcos, J.S., Romero, R., Carrasco, D., Moreno, V., Valero, J.L., Lafitte, M., 2007. Implementation of new SAR change detection methods: super resolution SAR change detector. In: Proc. ENVISAT Symposium, Montreux, Switzerland. <<http://earth.esa.int/envisatsymposium/proceedings/sessions/5E2/461545ro.pdf>> (last access 17.02.14).
- Marino, A., Cloude, S.R., Lopez-Sanchez, J.M., 2013. A new polarimetric change detector in radar imagery. *IEEE Trans. Geosci. Remote Sens.* 51 (5), 2986–3000.
- McNairn, H., Kross, A., Lapen, D.R., Caves, R., Shang, J., 2014. Early season monitoring of corn and soybeans with TerraSAR-X and RADARSAT-2. *Int. J. Appl. Earth Obs. Geoinf.* 28, 252–259.
- Metz, A., Marconcini, M., 2014. A novel system for monitoring grassland dynamics based on polarimetric SAR data. In: Proc. 10th European Conference on Synthetic Aperture Radar 2014, Berlin.
- Moreira, A., Prats-Iraola, P., Younis, M., Krieger, G., Hajnsek, I., Papathanassiou, K., 2013. A tutorial on synthetic aperture radar. *IEEE Geosci. Remote Sens. Magazine (GRSM)* 1 (1), 6–43.
- Navarro-Sánchez, V.D., Lopez-Sánchez, J.M., 2014. Spatial adaptive speckle filtering driven by temporal polarimetric statistics and its application to PSI. *IEEE Trans. Geosci. Remote Sens.* 52 (8), 4548–4557.
- Ossikowski, R., 2008. Interpretation of nondepolarizing Mueller matrices based on singular-value decomposition. *J. Opt. Soc. Am. A* 25 (2), 473–482.
- Ossikowski, R., Anastasiadou, M., Ben Hatir, S., Garcia-Caurel, E., De Martino, A., 2008. Depolarizing Mueller matrices; how to decompose them? *Physica Status Solidi A* 205 (4), 720–727.
- Praks, J., Colin-Koeniguer, E., Hallikainen, M.T., 2009. Alternatives to target entropy and alpha angle in SAR polarimetry. *IEEE Trans. Geosci. Remote Sens.* 47 (7), 2262–2274.
- Raney, R.K., 1998. Principles & Applications of Imaging Radars, . third ed.. In: Henderson, F.M., Lewis, A.J. (Eds.), *Manual of Remote Sensing* third ed., vol. 2 Wiley, p. 77.
- Raney, R.K., 2007. Hybrid-polarity SAR architecture. *IEEE Trans. Geosci. Remote Sens.* 45 (11), 3397–3404.
- Raney, R.K., 2011. A perspective on compact polarimetry. *IEEE Geosci. Remote Sens. Soc. Newsletter*, 12–18.
- Schmitt, A. 2012. Change Detection on Multi-Temporal and Multi-Polarized Radar Acquisitions (Language German, original title: Änderungserkennung in multitemporalen und multipolarisierten Radaraufnahmen). PhD thesis. Karlsruhe Institute of Technology, Germany.
- Schmitt, A., Brisco, B., 2013. Wetland monitoring using the curvelet-based change detection method on polarimetric SAR imagery. *Water* 5, 1036–1051.
- Schmitt, A., Wessel, B., Roth, A., 2010. Curvelet-based change detection on SAR images for natural disaster mapping. *Photogr., Fernerkundung, Geoinform.* 6, 463–474.
- Schmitt, A., Wessel, B., Roth, A., 2014. An innovative curvelet-only-based approach for automated change detection in multi-temporal SAR imagery. *Remote Sens.* 6 (3), 2435–2462. <http://dx.doi.org/10.3390/rs6032435>.
- Shan, Z., Wang, C., Zhang, H., Chen, J., 2011. H-alpha decomposition and alternative parameters for dual polarization SAR data. In: Proc. PIERS, Suzhou, China.
- Touzi, R., 2002. A review of speckle filtering in the context of estimation theory. *IEEE Trans. Geosci. Remote Sens.* 40 (11), 2392–2404.
- Touzi, R., 2007. Target scattering decomposition in terms of roll-invariant target parameters. *IEEE Trans. Geosci. Remote Sens.* 45 (1), 73–84.
- Touzi, R., Boerner, W.M., Lee, J.S., Lueneburg, E., 2004. A review of polarimetry in the context of synthetic aperture radar: concepts and information extraction. *Can. J. Remote Sens.* 30 (3), 380–407.
- Touzi, R., Deschamps, A., Rother, G., 2009. Phase of target scattering for wetland characterization using polarimetric C-band SAR. *IEEE Trans. Geosci. Remote Sens.* 47 (9), 56–67.
- Ullmann, T., Banks, S.N., Duffe, J., Roth, A., Schmitt, A., Baumhauer, R., Dech, S., 2013. Classification of coastal arctic land cover by means of TerraSAR-X dual co-polarized data (HH/VV). In: Proc. 5th TerraSAR-X Science Team Meeting, Oberpfaffenhofen, Germany.
- Unal, M.H., Ligthart, L.P., 1998. Decomposition theorems applied to random and stationary radar targets. *Progr. Electromagn. Res.* 18, 45–66.
- Yamaguchi, Y., Moriyama, T., Ishido, M., Yamada, H., 2005. Four-component scattering model for polarimetric SAR image decomposition. *IEEE Trans. Geosci. Remote Sens.* 43 (8), 1699–1706.